5-2024

Multi-Scale Modeling of Selective Laser Sintering: From Manufacturing Process and Microstructure to Mechanical Performance in Semi-crystalline Thermoplastics

Cameron Zadeh
ozadeh@clemson.edu

MULTI-SCALE MODELING OF SELECTIVE LASER SINTERING: FROM MANUFACTURING PROCESS AND MICROSTRUCTURE TO MECHANICAL PERFORMANCE IN SEMI-CRYSTALLINE THERMOPLASTICS

A Dissertation
Presented to
the Graduate School of
Clemson University

In Partial Fulfillment
of the Requirements for the Degree
Doctor of Philosophy.
Automotive Engineering

---

by
Cameron Zadeh
May 2024

Accepted by:
Dr. Srikanth Pilla, Committee Chair
Dr. Gang Li
Dr. Rahul Rai
Dr. Morteza Sabet

ABSTRACT

Selective laser sintering is an additive manufacturing process that opens many design possibilities but is limited in its reliability and reproducibility. Numerical simulations validated by experimental data yield insights into the process and resulting part properties, allowing users to make more informed decisions. In this dissertation, a model for the process and microstructure is developed and validated, followed by a coupling to mechanical models to predict part performance. Further developments include a new addition of a reaction kinetics model to the process model to describe the interplay between thermal degradation and melt pool properties, and an exploration of the parameter space with respect to different laser beam profiles.

DEDICATION

I dedicate this manuscript to my family, friends, advisors, colleagues, teachers, professors, mentors, and everyone else who supported me on this journey.

ACKNOWLEDGMENTS

Research primarily supported as part of the AIM for Composites, an Energy Frontier Research Center funded by the U.S. Department of Energy (DOE), Office of Science, Basic Energy Sciences (BES), under Award #DE-SC0023389 (computational modeling, data analysis) and by the Army Research Laboratory and was accomplished under Cooperative Agreement Number W911NF2020237 (experimental characterization).

TABLE OF CONTENTS

Table of Contents (Continued) Page

LIST OF TABLES

LIST OF FIGURES

List of Figures (Continued)

Figure Page

List of Figures (Continued)

Figure Page

CHAPTER ONE

INTRODUCTION

Additive manufacturing (AM), commonly known as 3D printing, is a manufacturing process that provides unprecedented design flexibility and the ability to produce complex geometries with improved efficiency. Among the seven major categories of AM, Powder Bed Fusion (PBF) stands out as one of the earliest and most versatile. PBF is adept at processing a wide range of materials, including polymers, metals, ceramics, and composites [1], [2]. In this process, powder layers are fused together layer by layer using energy sources, such as lasers or electron beams.

Selective Laser Sintering (SLS), a pioneering PBF technique developed at the University of Texas at Austin, remains a widely adopted method [1]. SLS is particularly notable for its use of polymers, with Polyamide 12 (PA12) being the most prevalent due to its superior characteristics like low processing temperatures, minimal laser power requirements, and high precision in the final product [3]. SLS is used for serial production of structural components in the automotive and aerospace industries, among others.

However, the broad adoption of SLS faces challenges, primarily due to uncertainties surrounding part quality, which is attributed to the complexity of the process and a not fully understood array of physical mechanisms [4], [5]. The quality of SLS parts is influenced by numerous parameters, approximately 100, with about 20 having a primary effect on the outcome [6]–[8]. These include laser power, scan velocity, scan spacing, layer height, chamber temperature, powder properties, and build orientation

[6]–[8]. The laser parameters are crucial as they determine the energy imparted to the powder bed, which in turn affects the degree of particle melting and fusion, significantly influencing the mechanical properties of the final product [8], [9].

The relationship between these parameters is often conceptualized through the lens of energy density, which provides a simplified understanding of their combined effect. Volumetric energy density E_v, defined by Equation (1), encapsulates the interaction of laser power P, scan velocity v, scan spacing S, and layer height L [8], [10].

$$E_v = \frac{P}{\upsilon SL} \tag{1}$$

Studies by Caulfield et al. and others have established the critical role of energy density in determining part density and mechanical properties, highlighting the importance of maintaining appropriate energy density levels to prevent degradation while ensuring sufficient material fusion [8], [10]–[13].

Despite the insights gained from experimental studies, the trial-and-error approach to optimizing SLS process parameters is both costly and time-consuming [14]. This has led to the increasing relevance of computational modeling, particularly the finite element method (FEM), as a more efficient way to understand the SLS process. FEM models, which represent the powder as a continuum with uniform properties, have been instrumental in studying various aspects of SLS, including heat transfer, fluid flow, crystallization, and melting [14], [15].

Research Gap 1

Recent advancements in the modeling of SLS, such as those by Soldner et al., Li et al., and Mokrane et al., have contributed significantly to our understanding of the process. These models have explored various aspects, including nonisothermal crystallization, shrinkage, warpage, and densification [14]–[16]. However, a comprehensive model that integrates mechanical properties into the simulation of the SLS process remains a significant gap in the field (Table 1) [14]–[20].

Table 1: Literature review of process models for SLS.

Work	Laser Model	Crystall-ization	Densi-fication	Stress-Strain	Perform-ance
Bugeda et al. [1999]	✓	×	✓	×	×
Xin et al. [2017]	✓	×	✓	×	×
Soldner et al. [2021]	✓	✓	×	×	×
Mokrane et al. [2018]	✓	✓	✓	×	×
Ganci et al. [2017]	✓	×	×	×	×
Amado et al. [2015]	×	✓	×	×	×
Li et al. [2020]	✓	✓	✓	×	×

Addressing this gap, the present study introduces a FEM-based multiscale-multiphysics framework to capture the behavior of semicrystalline SLS PA12 throughout the various stages of the SLS process, from powder melting to non-isothermal crystallization and through final part performance. This framework enables the prediction of how laser power influences the properties and performance of SLS parts, offering a novel approach to improve material compositions and manufacturing processes for complex shapes.

A wide range of physical phenomena are incorporated to model the SLS process, such as heat conduction, convection, radiative transfer, nonisothermal crystallization, melting, and sintering. A novel aspect is the integration of Beer-Lambert's law with a line input model for laser interaction. The ability to predict porosity variations in response to different laser powers makes it a unique contribution to the field. A multi-mechanism mechanical model, developed by Tatiana Stepanova (Clemson University), accounts for crystalline and amorphous phases using numerical homogenization for the periodic porosity throughout the material. This study not only enhances our understanding of the SLS process for polymers but also sets the stage for future research and applications. While similar frameworks have been developed for metal laser sintering, the distinctive thermal, microstructural, and rheological characteristics of polymers necessitate a different approach, as demonstrated in this work [7]. Through this research, we aim to bridge the gap in process-structure-property-performance understanding, ultimately paving the way for more efficient and effective use of SLS in various industrial applications.

Research Gap 2

Although energy density must be high enough to achieve sufficient part density and mechanical strength, high processing temperatures can inadvertently degrade the polymer. Energy density exhibits a positive correlation with part density up to a certain threshold. Beyond this point, further increases in energy density do not enhance, and may even reduce, part density due to thermal degradation [21], [22]. This degradation primarily occurs through post-condensation, which not only increases the polymer's molecular weight, making the material more viscous and less capable of coalescing effectively but also releases water, further complicating the sintering process (Figure 1) [23]–[29]. Specifically, under the nitrogen atmosphere commonly used in SLS and at the processing temperatures typical of this method, polyamides are known to undergo significant post-condensation [26]. Polyamides follow single-stage, first-order chemical reaction that can be precisely quantified using thermogravimetric analysis (TGA) [30].

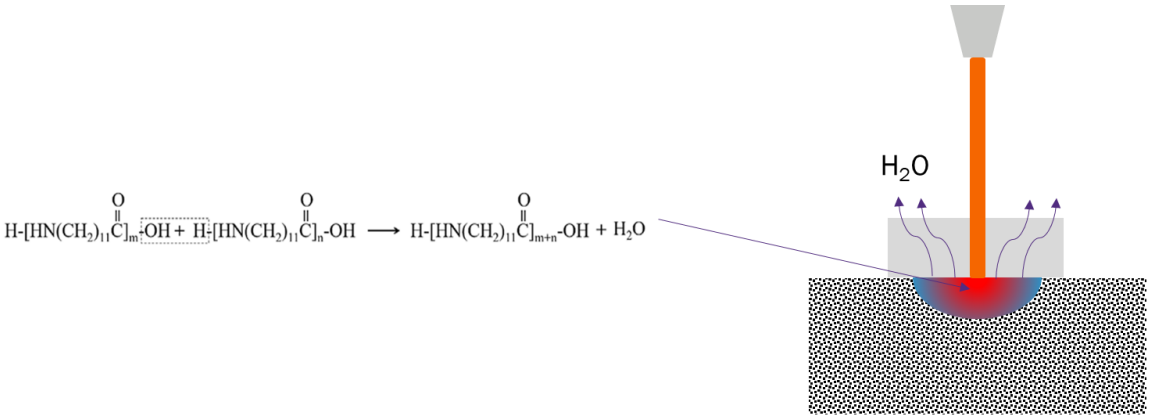

Figure 1: Post-condensation within the melt pool during SLS [23].

Recent advancements in heat transfer models for SLS have significantly improved our understanding of melt pool dynamics (Table 2) [14]–[16], [18], [31], [32].

For metal sintering, comprehensive models exist that account for various phenomena such as vaporization, mass loss, energy dissipation, recoil pressure, and alterations in chemical composition [7], [33], [34].

However, a critical gap remains in our understanding of thermal degradation mechanisms within the melt pool, especially concerning thermoplastics like polyamides. This gap in knowledge is significant because understanding the impact of thermal degradation on melt pool temperature is crucial for predicting and controlling microstructure and mechanical properties.

Given this context, the specific research gap addressed in this chapter is the impact of post-condensation reactions of polyamide 12 (PA12) on the thermal characteristics of the melt pool. While the effects of post-condensation on molecular weight and viscosity are well understood, it is unknown how a loss of mass from the reaction affects melt pool temperature.

Table 2: Literature review of heat transfer models in SLS.

Work	Laser Model	Cond-uction	Convec-tion	Emission	Radiator	Degradation
Childs et al. [1999]	✓	✓	×	×	×	×
Dong et al. [2009]	✓	✓	✓	✓	×	×
Xin et al. [2017]	✓	✓	✓	✓	×	×
Mokrane et al. [2018]	✓	✓	✓	✓	×	×

Li et al. [2020]	✓	✓	✓	×	×	×
Soldner et al. [2021]	✓	✓	✓	✓	✓	×

Research Gap 3

In SLS, a high manufacturing speed is desired but not at the expense of part quality. Maintaining processing temperatures below the critical threshold of 320 °C is essential to mitigate thermal degradation and preserve part quality [21]. Over 96% of SLS processes operate with laser powers no greater than 100 W to ensure high quality and resolution [35]. However, laser beam shaping is a possible way to transcend those constraints.

By changing the intensity distribution of the laser, temperature gradients can be reduced, leading to lower temperatures. Then, higher laser powers and scan velocities can be used leading to faster builds without sacrificing part quality [35].

While Gaussian beams have the best focusing properties and are widely used, they produce high temperature gradients in the substrate and high temperatures in the center [35], [36]. Alternative beam shapes, such as elliptical, top-hat, ring, and Bessel beams, emerge as viable solutions to the challenges posed by Gaussian beams, potentially revolutionizing SLS processing strategies.

The exploration of non-Gaussian beam profiles, notably ring and top-hat beams, has been documented (Table 3) to extend the processing window and increase build rates

in metal Laser Powder Bed Fusion (LPBF) [35], [37]–[39]. These beams are characterized by shallower temperature gradients within the melt pool, an attribute particularly advantageous for LPBF, where maintaining processing temperatures within a precise range is crucial. Furthermore, elliptical and Bessel beams have been associated with the formation of more equiaxed microstructures in metal LPBF, suggesting their influence extends beyond processing parameters to affecting the microstructural integrity of the final parts [40]–[44].

Despite these advancements in metal LPBF, a research gap exists regarding the application and effects of varied laser beam profiles on the SLS of semi-crystalline thermoplastics. Given the distinct thermal and physical properties of polymers—such as lower thermal diffusivity, lower viscosity, different optical properties, and differing mechanisms of microstructure formation—there is a compelling need for dedicated research to understand how these alternative beam profiles influence the melt pool dynamics, processing windows, and ultimately, the microstructure of polymer-based SLS parts.

This chapter seeks to address a critical research gap: assessing the impact of different laser beam profiles on the melt pool characteristics, processing windows, and microstructural outcomes in SLS processes involving semi-crystalline polymers. The overarching goal is to discern whether alternative beam shaping strategies can replicate the successes observed in metal additive manufacturing, thereby enhancing the efficiency and quality of polymer SLS processes.

Table 3: Literature review of beam profile studies in LPBF.

Work	Material	Experi-mental	Num-erical	Ring	Top-Hat	Elliptical	Bessel
Protasov et al. [2017]	316L SS	×	✓	✓	✓	×	×
Metel et al. [2018]	CoCrMo Alloy	✓	×	✓	✓	×	×
Roehling et al. [2020]	316L SS	✓	×	×	×	✓	×
Matthews et al. [2020]	316L SS	✓	✓	×	×	✓	✓
Tumkur et al. [2020]	316L SS	✓	✓	×	×	×	✓
Shi et al. [2020]	316L SS	×	✓	×	×	✓	×
Grünewald et al. [2021]	AISI 316L	✓	×	✓	×	×	×
Grigoriev et al. [2022]	CoCr Alloy	×	✓	✓	✓	×	×
Moore et al. [2024]	304L SS	×	✓	✓	×	×	✓

Dissertation Structure

In this dissertation, I describe the development of an advanced process model for SLS and its validation with experimental data. In Chapter Two, the process model is integrated into a mechanical model to enable process-structure-property-performance

modeling. A thermal degradation model is developed and integrated into the process model in Chapter Three. Chapter Four explores the impact of different laser beam profiles on melt pool characteristics, processing windows, and microstructure.

CHAPTER TWO

PROCESS-STRUCTURE-PROPERTY-PERFORMANCE MODELING

Task 1 is to establish a process-structure-property-performance framework by using heat transfer, laser, sintering, and crystallization models to generate representative volume elements (RVEs) for use in mechanical and performance models. It begins with the process data card which consists of models for relaxation time, viscosity, viscoelastic sintering, bubble dissolution, melting, density, thermal conductivity, specific heat capacity, crystallization kinetics, and the laser. With these models, process simulations can predict porosity, which can be validated with experimental measurements. A representative volume element is generated and used as an input to mechanical and performance models (developed by Tatiana Stepanova).

Experimental Methods and Materials

Materials

The material utilized in this study is PA12, a semi-crystalline thermoplastic known for its advantageous properties in SLS applications. Accounting for approximately 95% of materials used in SLS processes, PA12's popularity in this domain can be attributed to its distinct physical characteristics [45]. Due to its high heat of melting, low melting temperature, low zero-shear viscosity, and low surface tension, it is extremely well suited for SLS processing, giving operators fine control over melting and sintering and enabling the production of nearly fully dense parts [46].

Our study specifically utilizes the commercial DuraForm ProX PA grade PA12 powder supplied by 3D Systems. To ensure consistency and repeatability all specimens

were printed using refreshed DuraForm ProX PA powder. This refreshed powder is a mixture of 40% virgin and 60% previously used powder as recommended by the manufacturer, critical to maintaining the material properties conducive for optimal SLS processing.

Selective Laser Sintering Process

The SLS process unfolds in three distinct stages, each critical to the quality of the final product. In preparation, the printing chamber is filled with nitrogen to prevent oxidation and degradation of the powder, ensuring consistent material properties [1].

1. **Sintering Stage**: In this stage, a CO_2 laser selectively melts the powder bed, defining the layer's geometry and density.

2. **Layering and Support**: After each scan, the build platform is lowered by 100 µm. A new powder layer is then evenly spread over the previous one using a counter-rotating roller. The non-sintered powder around the part provides the necessary support for complex structures.

These steps are repeated until the part is fully constructed. The layer-by-layer technique enables the creation of complex geometries.

3. **Cooling and Post-Processing**: After sintering, the chamber cools down to solidify the parts. Once cooled, the parts are extracted, and the unused powder is collected for reuse, enhancing process sustainability [47].

Process Parameters

This study utilized two SLS machines with similar capabilities, namely the SLS ProX 6100 and SLS ProX 380, both provided by 3D Systems, to fabricate specimens at varying laser powers.

1. **Initial Batch with SLS ProX 6100**: The initial set of specimens was produced using the SLS ProX 6100, adhering to the manufacturer's recommended optimal process parameters (see Table 4. List of SLS process parameters.). The primary focus for this batch was to establish a baseline with an optimal laser power set at 62 W.
2. **Variable Laser Power with SLS ProX 380**: To investigate the effects of different laser powers, the SLS ProX 380 was employed. This machine was used to fabricate additional specimens while maintaining all process parameters constant, except for the fill laser power. The fill laser power was varied across three settings: 31 W, 80 W, and 100 W, while the outline laser power was consistently maintained at 20 W. These variations are also detailed in Table 4.

Specimens were printed in the X-orientation (lying flat) in the dimensions of ASTM D638 Type I. All parts were post-processed by bead blasting and freshwater rinsing to remove loose powder and smooth the surface.

Table 4. List of SLS process parameters.

Fill Laser power (P)	31 W, 62 W, 80 W, 100 W
Fill Scan velocity (v)	12,700 mm/s
Outline Laser Power	20 W

Outline Scan Velocity	5,000 mm/s
Layer thickness (*L*)	0.1 mm
Scan spacing (*S*)	0.2 mm
Scanning direction	Alternating every layer
Preheating temperature	0-4.572mm = 130°C 4.572mm-6.35mm= 155° 6.35-13mm= 170.5

Scan Strategy

The laser scan strategy deployed in this study is multifaceted and is designed to maximize the precision and quality of the sintered parts. This strategy is executed in two main phases: fill scans and outline scans, as illustrated in Figure *2*.

1. **Fill Scans**: The initial phase involves the fill scans, where the bulk of the layer is sintered. Parameters governing this phase include laser power, scan velocity, and scan spacing, which is the center-to-center distance between adjacent fill scan lines. These settings are critical for ensuring uniform energy distribution and optimal melting of the powder.
2. **Outline Scans**: Following the fill scans, outline scans are performed to define the precise contours of the part. This phase is characterized by its own set of parameters: laser power, scan velocity, and offset distance. The offset distance is the center-to-center spacing between the fill and outline scans, crucial for achieving sharp edges and accurate part dimensions.

A key feature of the employed scan strategy is the use of SinterScan, which alternates the direction of the fill scans between the X and Y axes with each layer. This alternating pattern helps to mitigate residual stresses and promotes uniform part density. Additionally, the 'Sorted Fill' option is activated, enhancing the efficiency of the sintering process. This feature optimizes the laser's path by avoiding movements across voids larger than 6.35 mm unless necessary. By reducing the time spent traversing empty spaces, the process becomes more time-efficient without compromising part quality.

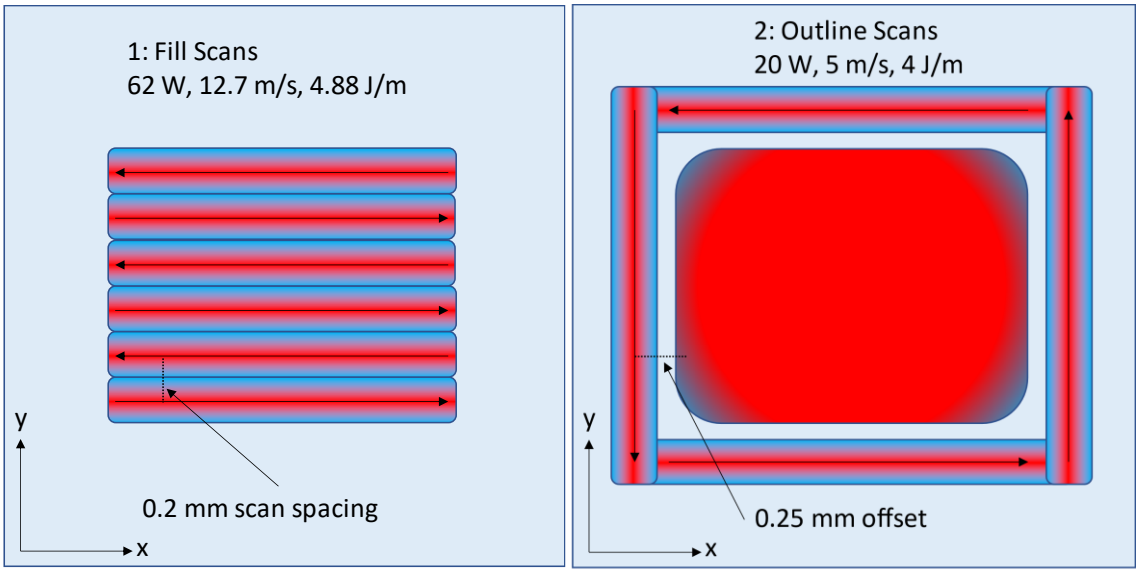

(a) (b)

Figure *2*. Scan strategy for (a) fill and (b) outline scans.

Characterization Methods

Differential Scanning Calorimetry

Thermal properties of both the DuraForm ProX PA powder and the SLS specimens were evaluated using two DSC instruments: the DSC 250 and the DSC Q20, provided by TA Instruments, New Castle, DE, USA. Data analysis was conducted using

TRIOS software version 5.1.1.46572 (TA Instruments) and MATLAB R2021a (version 9.10.0.1739362, MathWorks, Natick, MA, USA), facilitating interpretation of the thermal behavior of the materials.

Specific Heat Capacity

The specific heat capacity was determined following the ASTM E2716-23 standard for modulated temperature DSC tests. The procedure involved a modulation period of 120 seconds, a temperature amplitude of 1.0 °C, and a heating ramp rate of 3 °C min^{-1}. The reversing heat flow measured during these tests was divided by the heating rate to derive the reversing heat capacity [48]. The sample, consisting of DuraForm ProX PA powder at a 40% refresh ratio, weighed 8.195 mg and was placed in a Tzero Aluminum pan sealed with a hermetic lid for testing.

Heat of Melting and Crystallinity

For these measurements, samples with a mass of 9±1 mg were heated at 10 °C min^{-1} past their melting point, in accordance with ISO 11357-3 standards. The heat of melting was calculated using TRIOS software by employing peak integration against a sigmoidal curve. This heat of melting data was then used to ascertain the absolute degree of crystallinity, expressed as a mass fraction, utilizing the known heat of melting for 100% crystalline PA12 (209.3 J g^{-1}) and equation (2) [49], [50].

$$\chi = \frac{\Delta H_{sample}}{\Delta H_{100\%\ crystalline}} \tag{2}$$

Sample preparation included virgin, refreshed, and aged powder—the latter collected post-printing of the tensile specimens—as well as samples from the central

portion of these specimens. To ensure analysis consistency, tensile samples were bisected along the central axis (Figure 3), and thin sections were extracted from the inner regions of the cross-section, deliberately excluding any surface material.

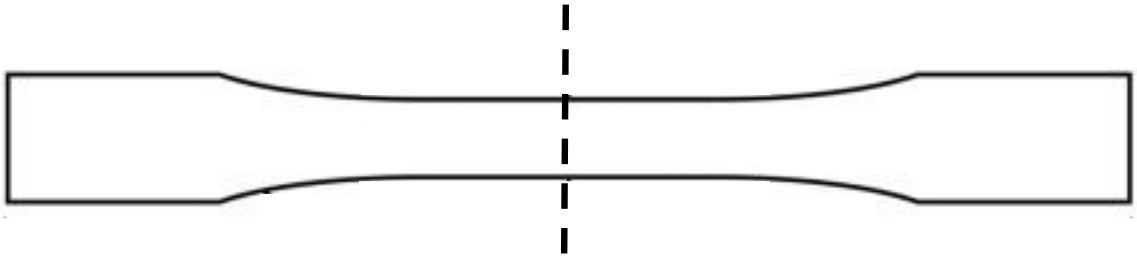

Figure 3: Schematic of axis of bisection for tensile specimens.

Crystallization Kinetics

The study of PA12 crystallization kinetics was conducted in accordance with ISO 11357-7 guidelines. To begin, powder samples with a mass of 3±1 mg were selected for analysis. These samples underwent a controlled heating process, where they were heated at 10 °C min^{-1} up to 230 °C. Upon reaching this temperature, the samples were maintained at a constant temperature for 5 minutes to ensure complete melting. Following the melting phase, the methodology transitioned to isothermal crystallization tests. During these tests, the molten samples were rapidly cooled at 200 °C min^{-1} rate to reach the target isothermal crystallization temperature, T_c. A range of T_c values was explored to understand the crystallization behavior at different temperatures comprehensively. The specific temperatures investigated were 160, 162, 164, 166, and 168 °C. Once each sample reached its designated T_c, the isothermal condition was maintained until the heat flow signal stabilized back to the baseline or sufficient time had passed according to the ISO standard.

Micro-CT

High-resolution imaging of the tensile specimens was conducted using a Quantum GX-2 Micro-CT scanner from PerkinElmer, based in Waltham, MA, USA. The specimens were scanned with a resolution of 20 µm. Operating parameters for the scans included an x-ray voltage of 90 kV and an amperage of 88 µA. The focus of the scanning was on the center region of the specimens as indicated in Figure 3.

After scanning, the Micro-CT images were reconstructed into three-dimensional models using DataViewer software version 1.5.6.2 from Bruker microCT, Kontich, Belgium. During this reconstruction, the object was aligned with the viewing axes, and a specific volume of interest was selected for analysis. This selection process intentionally excluded the surfaces and edges of the specimens to mitigate the influence of surface roughness on the imaging results. Images corresponding to this volume of interest were then extracted from three distinct viewing axes: coronal, sagittal, and transverse. Images from the coronal view represent X-Y planes spaced along the Z-axis of the part, which is the direction of layer deposition. This specific orientation was chosen to enable the detection of layer-wise variations in porosity, as other viewing planes did not exhibit significant trends in porosity perpendicular to the layer deposition axis.

For the quantitative analysis of porosity, ImageJ software (Java 1.8.0_345) from the National Institutes of Health, Bethesda, MD, USA, was utilized. The software was configured with custom macros to analyze entire image sets, employing local and global thresholding methods to calculate area percentage porosity. In local thresholding, unique threshold values were automatically determined for each image to calculate the area

percentage. Conversely, global thresholding used a uniform threshold value across all images in a set, determined by the statistical mode of the local threshold values. The average area percentage derived from global thresholding served as a representative measure of the sample's porosity, following the principle of Delesse [51].

Density Measurements

Density measurements of the specimens were conducted on rectangular sections extracted from the gauge section of the bisected specimens. Each section was prepared with a target length of 19±2 mm. Precise dimensions—length, width, and thickness—of these samples were determined using calipers. For mass determination, a precision scale capable of milligram measurements was employed.

The volume of each sample was calculated using the formula: volume = length × width × thickness. To obtain the density of each sample, the measured mass was divided by the calculated volume, according to the formula: density = mass / volume.

Model Framework

The multiscale-multiphysics framework (Figure 4) begins by simulating the SLS process at the microscale, considering various SLS process parameters. This simulation predicts the porosity distribution within the printed parts, a key factor influencing their mechanical properties. By bridging the gap between process simulation and mechanical behavior, multiscale-multiphysics framework offers a holistic view of SLS parts fabrication and performance. It provides a deeper understanding of how SLS process parameters influence the final mechanical properties of the printed parts, paving the way for optimized manufacturing processes and enhanced material design. The mechanical

model, developed by Tatiana Stepanova, considers the contributions of amorphous and crystalline phases of the material.

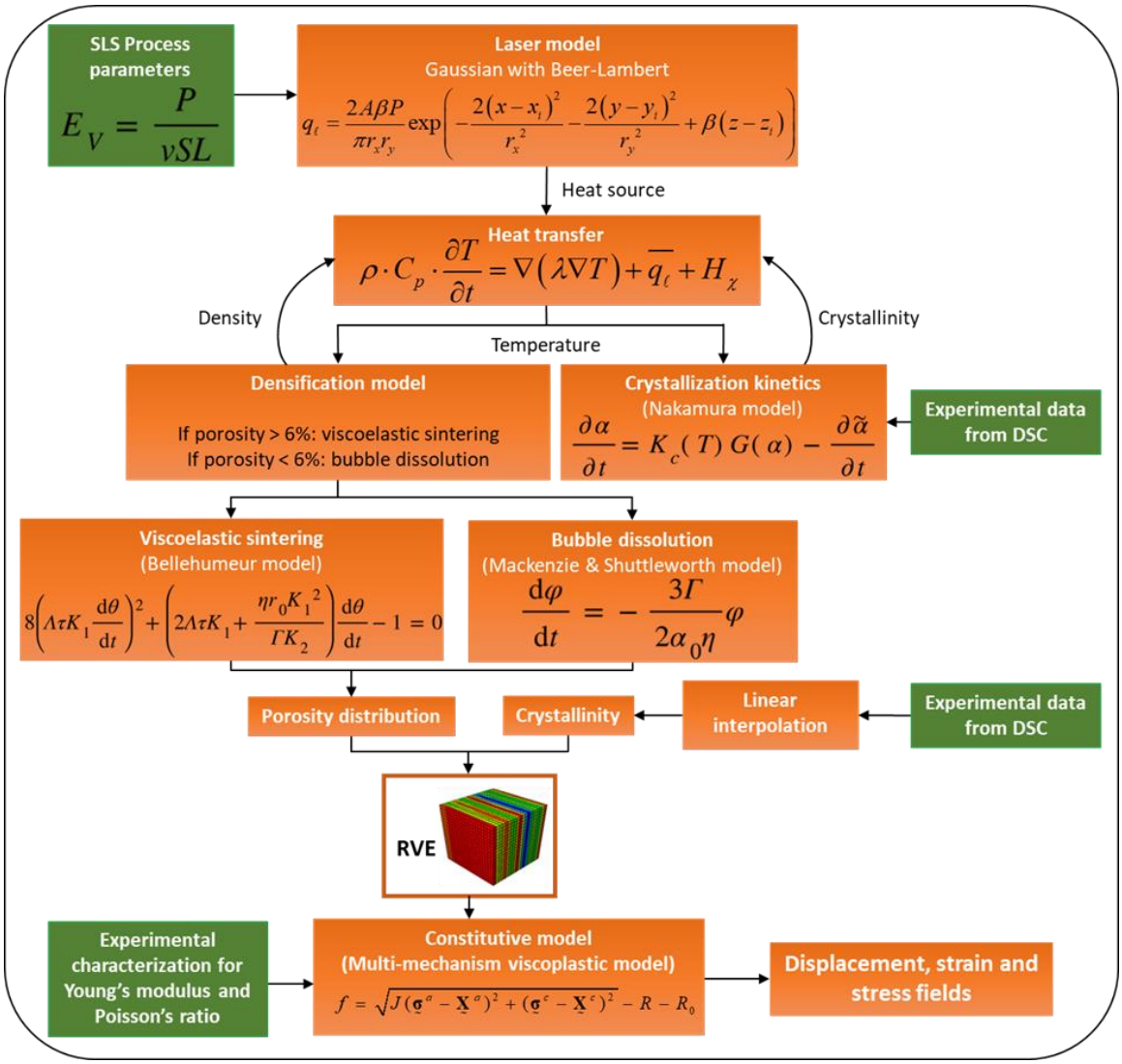

Figure 4. Modeling framework composed of process and mechanical models[1].

[1] This diagram has been jointly prepared with Tatiana Stepanova (May 2024 dissertation: PROCESS-STRUCTURE-PERFORMANCE MODELING FOR SEMICRYSTALLINE THERMOPLASTICS AND COMPOSITES).

Process Model

The process model is designed to predict the microstructural characteristics of parts fabricated through SLS, utilizing specific printing parameters as its foundation. This prediction is accomplished by integrating simulations of microstructure evolution, focusing on crystallization and densification, within a thermal model. The core mechanism of this thermal model is the radiative heating effect induced by the laser, which plays a pivotal role in the SLS process.

Central to heating is the laser model, which precisely delineates the laser's geometry and its dynamic movements as it interacts with the powder bed, providing the essential thermal energy required for sintering. The thermal model also considers the material's specific heat capacity, which is crucial for understanding the amount of heat necessary to alter the material's temperature, aside from phase changes.

A critical aspect of the simulation involves establishing the crystallinity of the powder, a factor that significantly influences the melting process due to its direct correlation with the heat absorption characteristics of the material. This is where the crystallization kinetics model comes into play, offering detailed insights into the melting and recrystallization behaviors of the material under the influence of laser heating.

Further, the model incorporates a densification mechanism, which is essential for capturing the sintering and bubble dissolution processes, leading to the coalescence of powder particles into a solid mass. The heat equation provides the unifying framework for these diverse simulations, which integrates the thermal interactions across the model.

The entire process model is implemented using MOOSE (Multiphysics Object-Oriented Simulation Environment) for finite element analysis (FEA). The model achieves a high level of versatility, allowing for an in-depth exploration of the process parameters' impact on the resulting microstructure of SLS-produced parts. Values of model parameters are summarized in Appendix A.

Laser Model

In the SLS process, the laser's intensity distribution is characterized by a Gaussian profile. This was first articulated in the context of welding simulations by Goldak et al. in 1984, who proposed a three-dimensional ellipsoidal Gaussian distribution model [52]. While this Gaussian ellipsoidal model, shown at the top left of Figure 5, is both simple and accurate, several changes were made to enhance its accuracy and implementation.

The velocity term is replaced with a system that reads time-paired coordinates from an input file, dictating the laser's position. The model's coordinate system is aligned such that the x and y axes are parallel to the powder bed surface, with the z-axis perpendicular to it. In this system, x_i denotes the x-coordinate of the laser's focus at a given time i, with x_{i+1} representing its position at the subsequent time step, and so forth.

The laser radii in the x and y directions, r_x and r_y, are fixed at 225 μm, aligning with the specifications of the SLS production systems used in this study. These radii define the Gaussian distribution such that the intensity at r_x and r_y are equal to $1/e^2$ times the maximum intensity.

Rather than a Gaussian distribution normal to the surface, this model incorporates the Beer-Lambert law to describe the decay of laser intensity as it penetrates the powder bed. This law has been validated through various studies for its accuracy in modeling laser intensity decay through powder [16], [53]–[56]. The extinction coefficient, β, is set at 9000 m^{-1}, derived from a combined experimental and numerical analysis of PA12 powder's optical properties subject to a CO_2 laser [53]. The absorptivity *A* (0.94), is set to the complement of PA12 powder's reflectivity when exposed to a CO_2 laser [57].

This form of the model (Figure 5 top right) produces the intensity distribution of the laser for an instant in time, setting a constraint on the duration of time steps in the simulation. Adhering to the Courant Friedrichs Lewy (CFL) condition necessitates that time steps are small enough to not skip elements in the mesh [58]. However, reducing the time step size to meet the CFL condition can result in an impractically high number of steps for the simulation. Addressing this limitation, Irwin et al. developed the line input model, allowing larger time steps [59]. To perform this transformation from q_ℓ to $\bar{q}_\ell$, the function is integrated over time respective to its traversal in the x direction and the time average is calculated (Figure 5 middle).

To enable the laser to move at any angle parallel to the powder bed surface, a rotation matrix is utilized. This matrix transforms the coordinate system to a new orientation where the polar angle of the laser is zero. The angle ω, representing the laser's directional change, is calculated using the current and next x and y positions. Then, the x_ω and y_ω coordinates replace the x and y coordinates in $\bar{q}_\ell$ and the final form of the model is obtained (Figure 5 bottom).

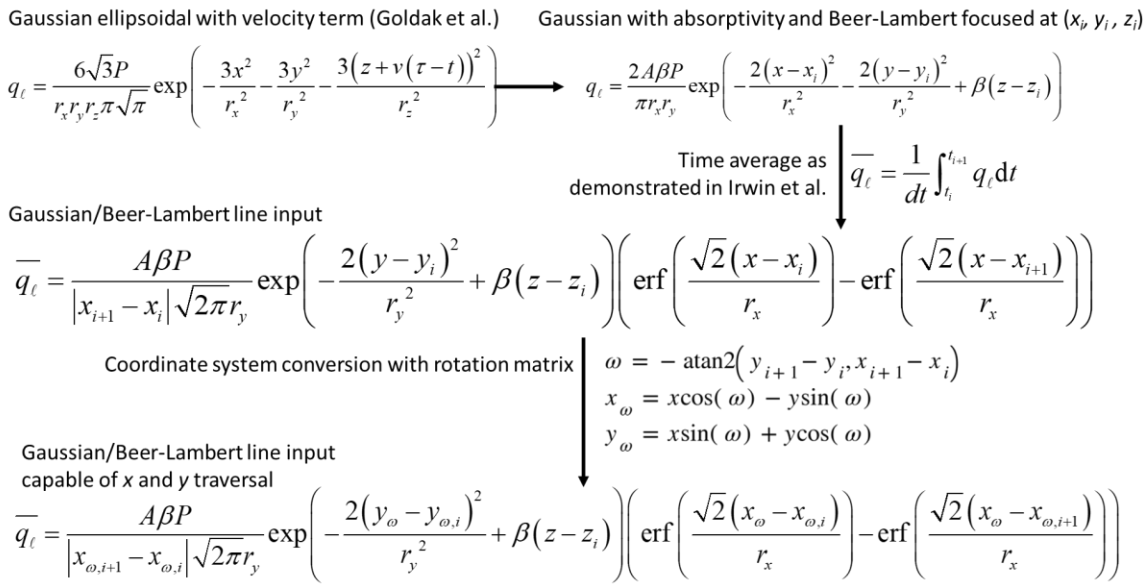

Figure 5. The transition from the Gaussian ellipsoidal model (top left), to the Gaussian Beer-Lambert model (top right), to the line input version (middle), and to the line input version capable of x and y traversal (bottom).

Specific Heat Capacity

The specific heat capacity of DuraForm ProX PA powder, with a 40% refresh ratio, was measured using a modulated temperature DSC test, as depicted in Figure 6. Prior to conducting this test, the DSC instrument underwent a thorough calibration to ensure precision. The calibration constants obtained were verified to be within acceptable ranges, thus ensuring that the measured reversing heat capacity accurately reflects the material's specific heat capacity.

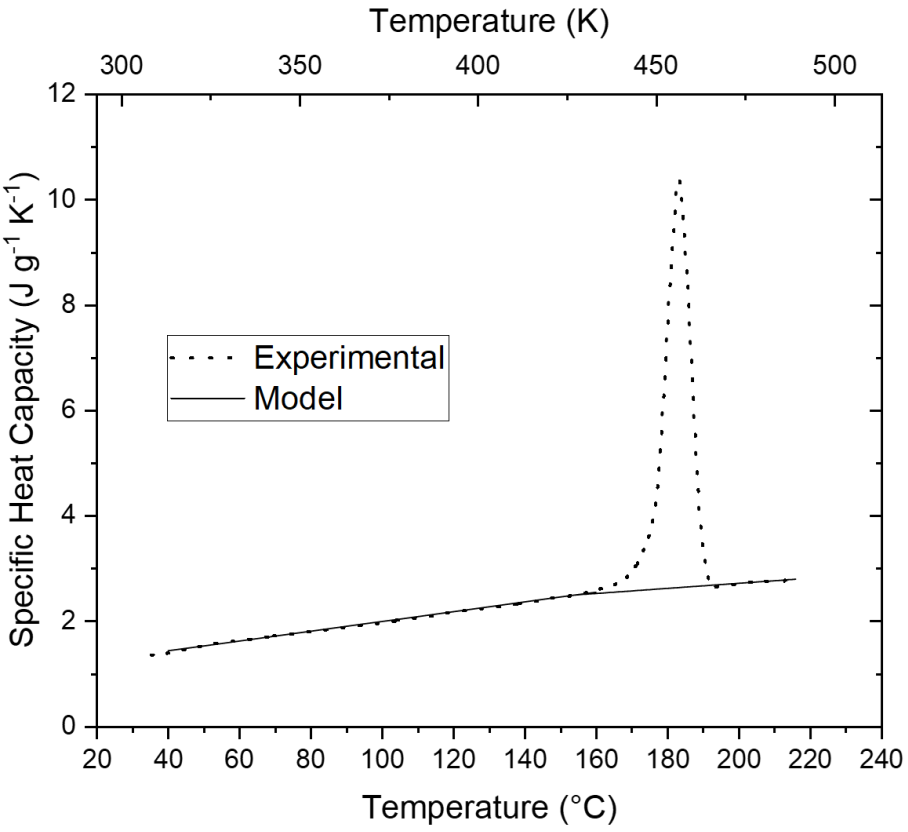

Figure 6. Specific heat capacity of refreshed PA12 powder through a temperature range as measured by modulated temperature DSC.

It is well-documented that the specific heat capacity of polymers, including PA12, varies depending on both temperature and crystallinity. This variability means that a single, constant value for specific heat capacity is insufficient to accurately represent the material's thermal properties. However, it is common to observe linear dependencies in both the solid and liquid phases of polymers [60]. For this study, data from the melting temperature range was excluded from the model calculations, as the heat of melting is considered separately. Instead, two distinct temperature ranges were selected for linear

modeling: the solid phase range from 40 °C to 160 °C and the liquid phase range from 194 °C to 216 °C.

Linear regression models were applied to these temperature ranges, yielding high correlation coefficients with R-squared values of 99.8% for the solid phase and 93.6% for the liquid phase. The two linear regression models seamlessly connect at their intersection point of 427.3281 K. The derived linear models express the specific heat capacity (in J g^{-1} K^{-1}) as a function of temperature in K. This relationship is formulated as

$$C_p(T) = \begin{cases} 0.0092711829 \cdot T - 1.4700038 & T < 427.3281\ K \\ 0.0048381976 \cdot T - 0.42433564 & T \geq 427.3281\ K \end{cases} \quad (3)$$

Powder Crystallinity

Table 5 provides a summary of the crystallinity and melting peak data for various states of PA12 powders. It is observed that both crystallinity and melting peaks exhibit slight variations depending on the aging state of the powder. Generally, the crystallinity of the powder hovers around 45%, while the melting peaks are consistently near 188 °C.

Table 5. Crystallinity and melting peak of PA12 powders.

Powder	First Heat Crystallinity [%]	Melting Peak [°C]
Virgin	45.5	187.6
40% Refreshed	45.8	188.1
Aged	44.9	188.1

In the context of the model, these empirical observations are utilized to define the initial absolute crystallinity χ_0 of the powder. For simulation, χ_0 is set to a consistent value of 0.45. This parameter is pivotal in accurately simulating thermal behavior and phase transitions of the PA12 powder during the SLS process.

Crystallization Kinetics

The crystallization model employed in this study is grounded in Avrami theory, which describes isothermal crystallization, and extended to non-isothermal conditions via the Nakamura model [61], [62]. The Avrami model

$$\alpha = 1 - \exp(-k(T)\, t^n) \tag{4}$$

encapsulates the isothermal crystallization process, employing the Avrami rate constant k and exponent n to estimate the relative crystallinity α [62]–[64].

For non-isothermal crystallization, the model utilizes

$$\alpha = 1 - \exp\left(-\left(\int_0^t K_c(T)\, \mathrm{d}\tau\right)^n\right) \tag{5}$$

based on the Nakamura model, employing the non-isothermal crystallization rate K_c as a function of temperature [61], [63], [64]. The relationship between the non-isothermal crystallization rate K_c and the Avrami rate constant k (also a function of temperature) is articulated as

$$K_c(T) = k(T)^{\frac{1}{n}} = \frac{\ln(2)^{\frac{1}{n}}}{t_{1/2}(T)} \tag{6}$$

introducing the crystallization half-time $t_{½}$ as a function of temperature [61], [63], [64]. Hoffman-Lauritzen theory provides further insights, linking the crystallization half-time $t_{½}$ with other parameters, as shown in Equation (7) [65]:

$$\left(\frac{1}{t_{1/2}}\right) = K_0 \exp\left(-\frac{U}{R\left(T - T_\infty\right)}\right) \exp\left(-\frac{K_g (T + T_0)}{2T^2 (T_0 - T)}\right) \quad (7)$$

where U denotes the activation energy for crystallization (6,270 J mol^{-1}), R is the universal gas constant (8.314 J mol^{-1} K^{-1}), T_∞ represents the lower temperature limit for crystallization ($T_\infty = T_g - 30$ °C = 30 °C), and T_0 is the equilibrium melting temperature [63]–[65]. Constants K_0 and K_g signify the growth and nucleation rate constants, respectively [63]–[65].

To determine the kinetic parameters (K_0, K_g, n, T_0), isothermal crystallization experiments were conducted at temperatures ranging from 160 to 168 °C. Figure 7 illustrates the heat flow during these experiments, where higher temperatures correlate with more gradual crystallization and lower, delayed peaks. The baselines were subtracted for clarity and analysis.

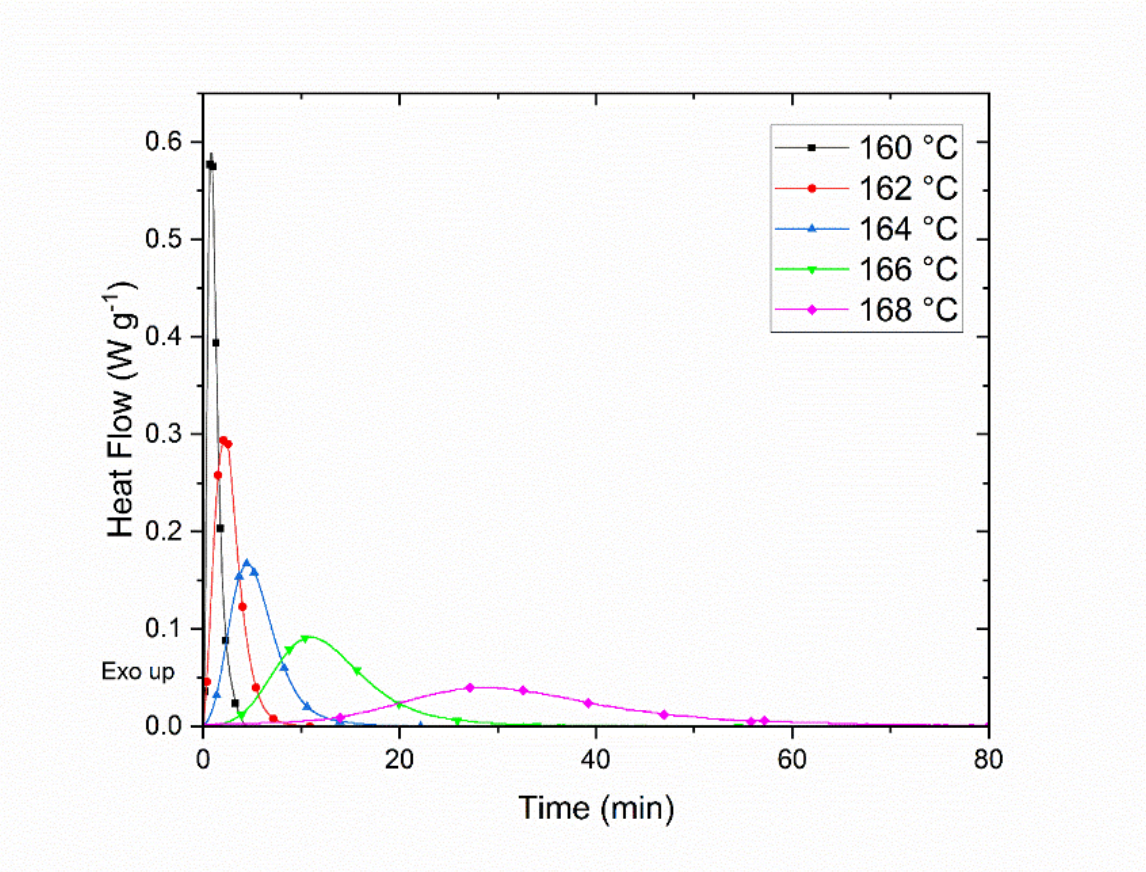

Figure 7. Normalized heat flow during isothermal crystallization at different temperatures.

The data from the isothermal runs are integrated to yield relative crystallinity α as a function of time, which is then linearized in Figure 8 [63], [64]. Trendlines are fit to the data, with a minimum R-squared value of 99%. The lower and upper bounds for relative crystallinity averaged at 7.14% and 90.23%, respectively. Data outside these bounds were

not considered for modeling. The slopes and intercepts of these lines provide the values for the Avrami exponent *n* and rate constant *k*, which are summarized in Table 6.

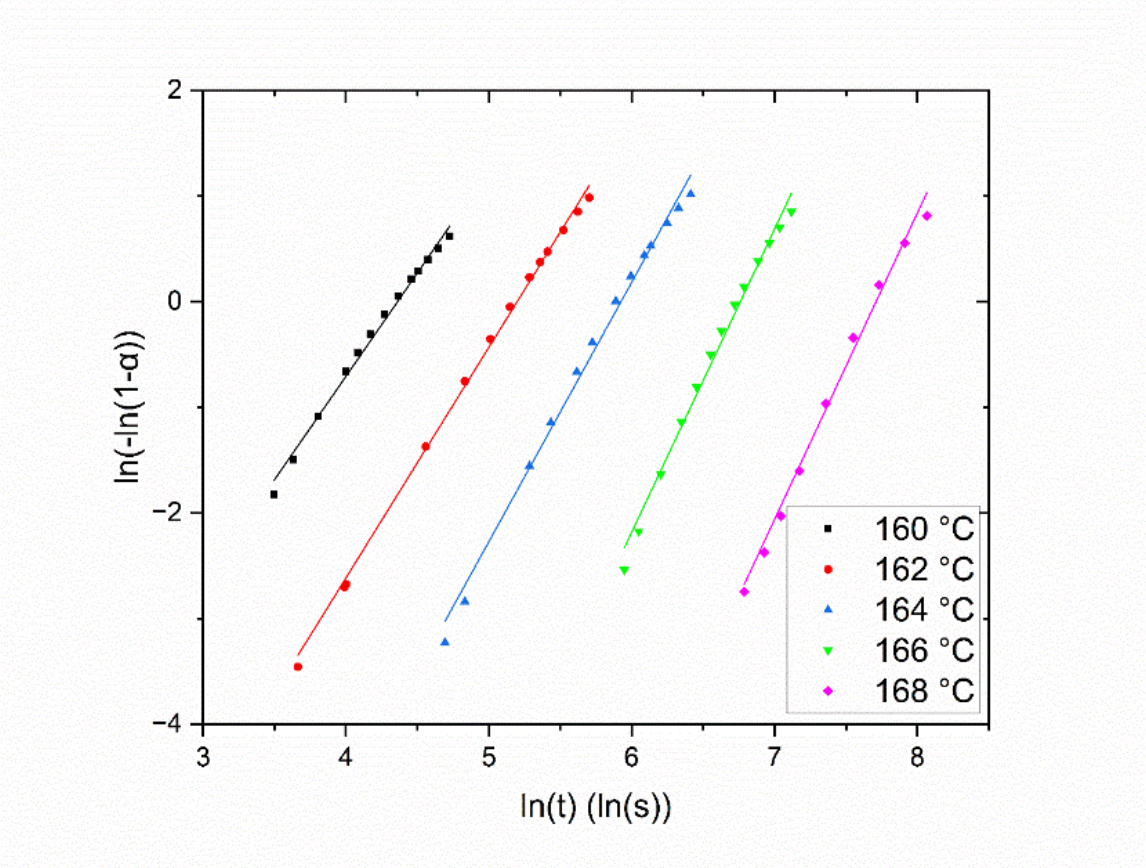

Figure 8. Linearization of isothermal crystallization at different temperatures with trendline fitting. Experimental values are represented by symbols while the linearization is represented by lines.

Table 6. Kinetic parameters for isothermal crystallization at different temperatures.

Isothermal Crystallization Temperature [°C]	Avrami exponent *n*	Avrami rate constant *k*	R^2	Crystallization Half Time [s]
160	1.95	1.976 e-04	0.9940	63.0

162	2.18	1.192 e-05	0.9980	149.4
164	2.46	4.808 e-07	0.9940	309.6
166	2.87	3.801 e-09	0.9917	733.8
168	2.90	1.932 e-10	0.9914	1,887.6

The Hoffman-Weeks theory was applied to correlate the isothermal crystallization temperature with the peak melting temperature of each sample [66]. The Hoffman-Weeks plot in Figure 9 demonstrates this correlation. The equilibrium melting temperature T_0, determined at the intersection point of the trendline with a 'y = x' line, is found to be 185.7 ℃, comparable to 193.2 ℃ and 192.4 ℃ found by Zhao et al. and Amado et al. for SLS PA12 powders [63], [67].

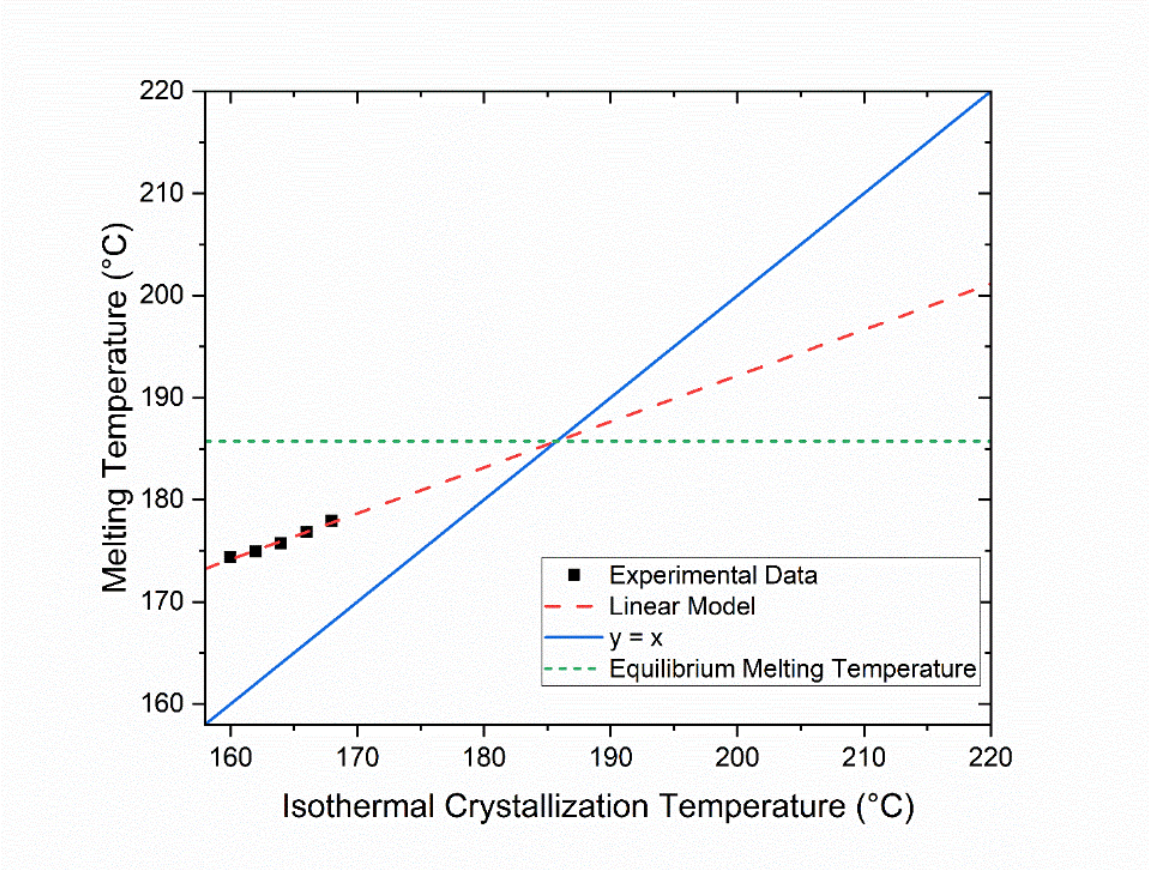

Figure 9. Hoffman-Weeks plot for equilibrium melting temperature of PA12.

To adapt these kinetic parameters for a nonisothermal model, the crystallization half-time's temperature dependency was captured empirically (Figure 10). The derived line, based on the Hoffman-Lauritzen theory, yields values for K_g and K_0 used in the Nakamura model [65], [68]. The values of K_g and K_0 are 96,730 K^2 and 33,927 s^{-1}, respectively.

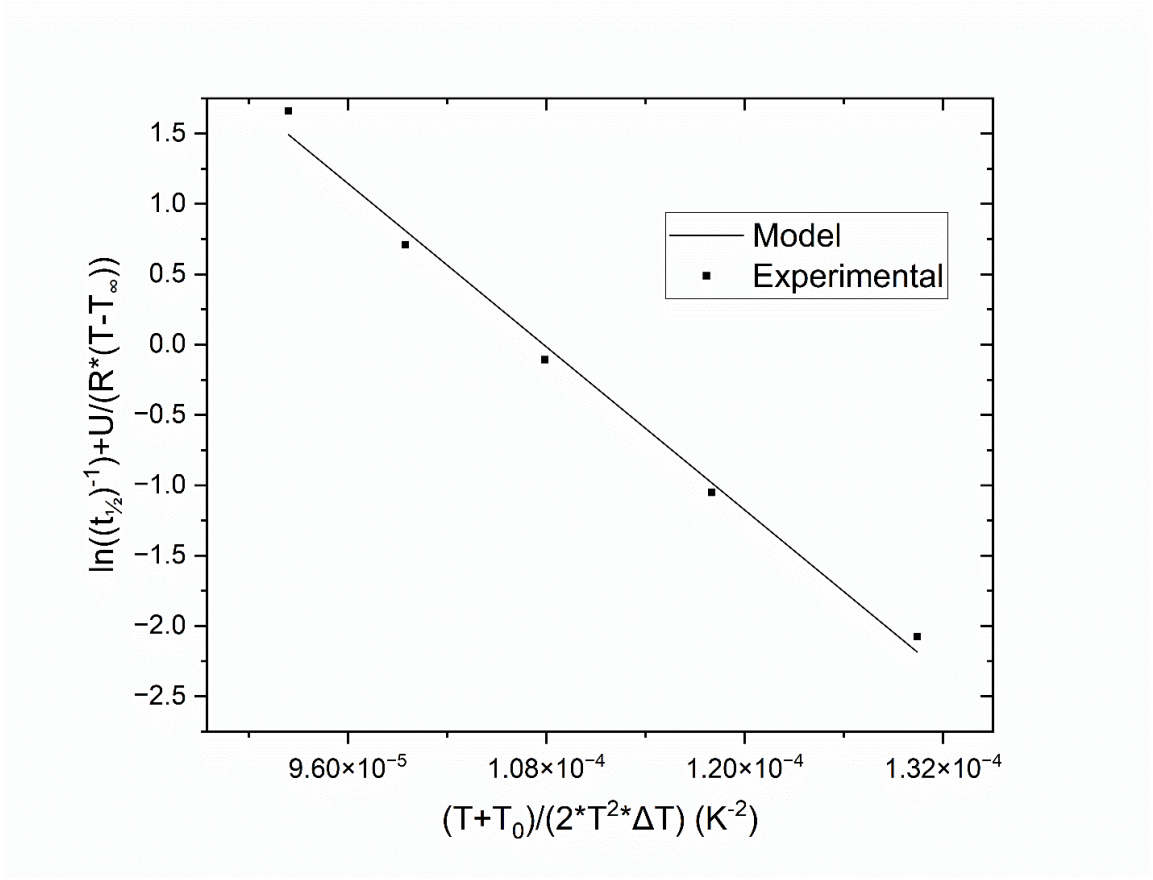

Figure 10. Linearization for nonisothermal kinetic parameters.

Figure 11 compares the measured crystallization half-times against model predictions, showing good agreement for most data, with some deviations at lower temperatures.

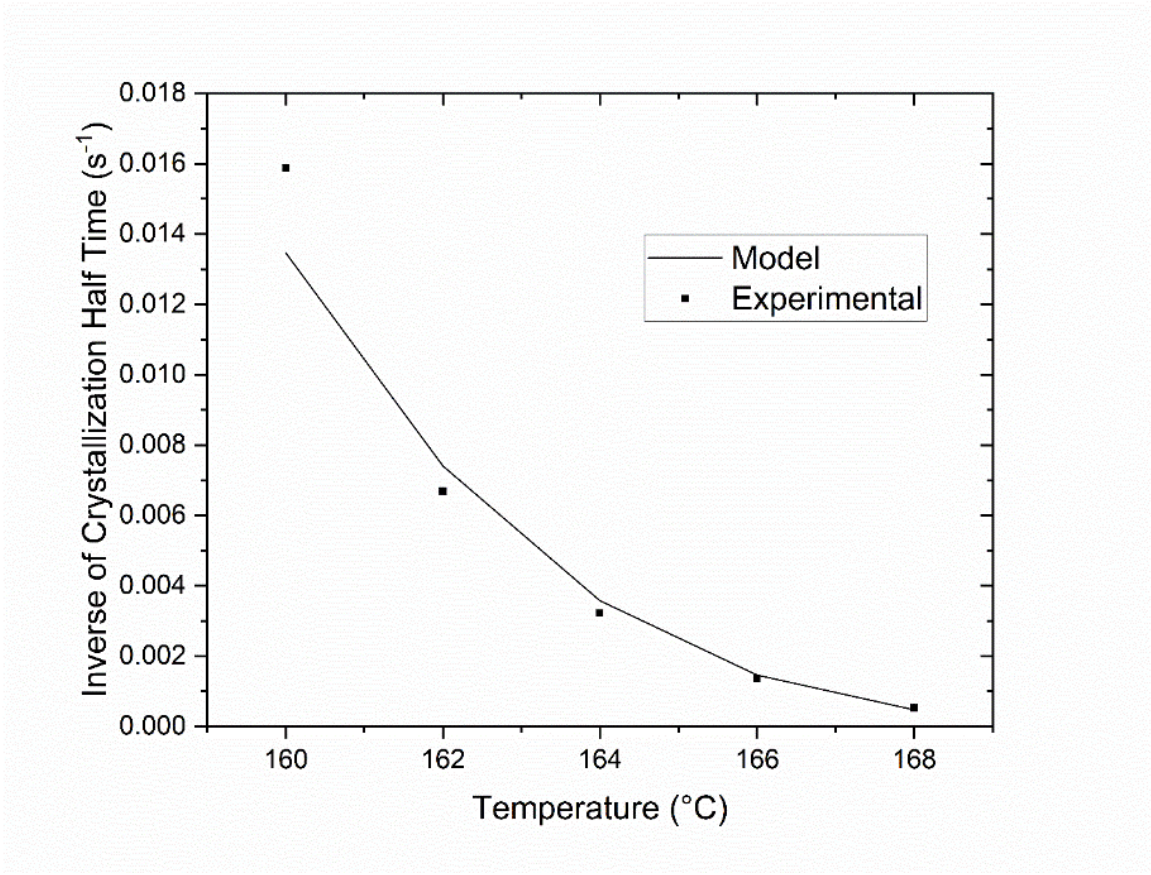

Figure 11. Inverse of crystallization half time with respect to temperature for experimental data and model predictions.

The overarching equation for crystallization and melting is given in Equation (8), with a modified crystallization rate defined in Equation (9) and the Nakamura function in Equation (10) [15]. A regularization term (Equation (11)) is introduced for melting [15]. In the model, the Avrami exponent, *n*, is set to 2.472, the average experimental value from Table 6.

$$\frac{\partial \alpha}{\partial t} = K_c(T)\, G(\alpha) - \frac{\partial \tilde{\alpha}}{\partial t} \tag{8}$$

$$K_c(T) = \ln(2)^{\frac{1}{n}} K_0 \exp\left(-\frac{U}{R\left(T - T_\infty\right)}\right) \exp\left(-\frac{K_g(T + T_0)}{2T^2(T_0 - T)}\right) \tag{9}$$

$$G(\alpha) = n(1-\alpha)\left(-\ln(1-\alpha)\right)^{1-\frac{1}{n}} \tag{10}$$

$$\frac{\partial \tilde{\alpha}}{\partial t} = \frac{\alpha}{dt}\left(1-\left(0.5\left(\tanh\left(0.5(454.3-T)\right)\right)+1\right)\right) \tag{11}$$

The Nakamura model (solid lines), along with the calculated parameters, closely aligns with experimental values (symbols) at different temperatures, as seen in Figure 12.

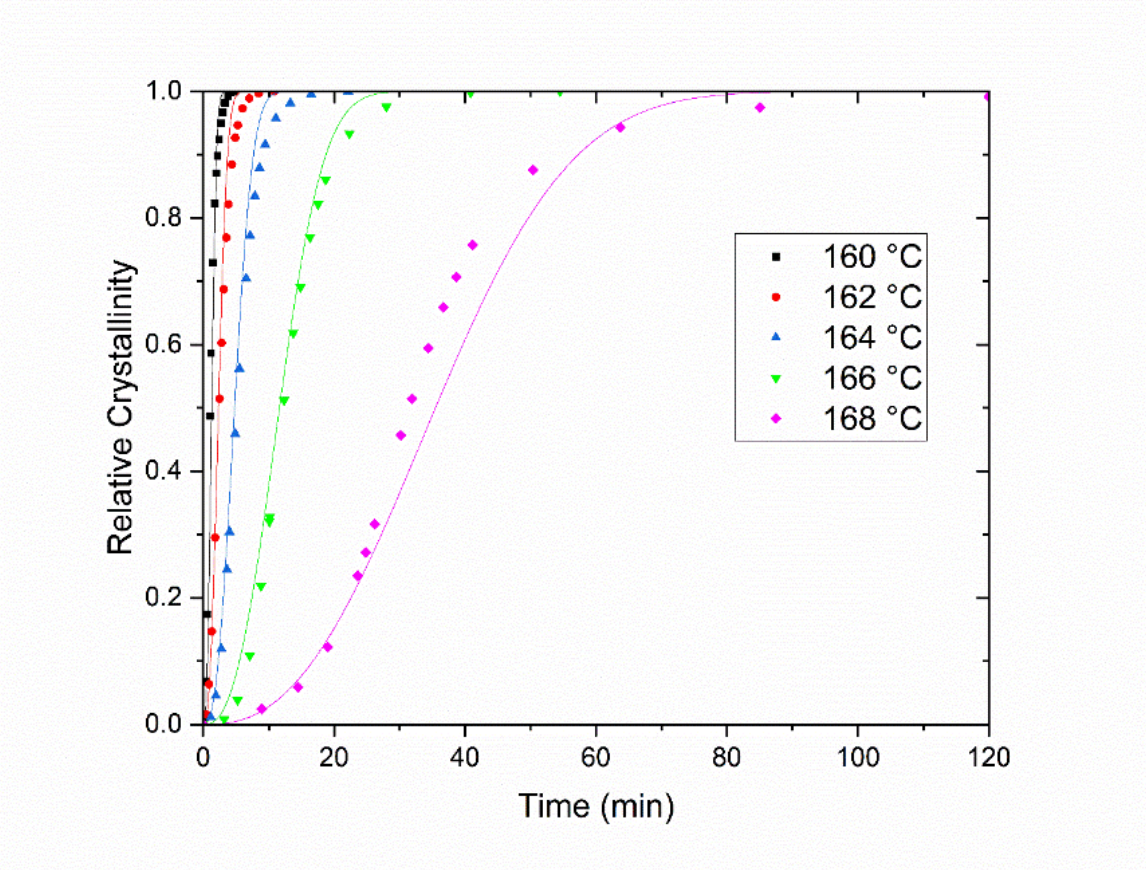

Figure 12. Relative crystallinity at different isothermal temperatures of experimental data (symbols) and Nakamura model predictions (solid lines).

The crystallization model is solved using the Explicit Euler method to obtain the relative crystallinity α. The relationship between relative crystallinity α and absolute crystallinity χ is given by

$$\chi = \alpha \cdot \chi_{max} \tag{12}$$

where χ_{max} is the maximum absolute crystallinity. The value of χ_{max} is informed by the crystallinity of tensile specimens printed at different laser powers and is set at 30%. The initial value of crystallinity, χ_0, is greater than χ_{max} because the powder is produced by solution precipitation, creating a highly crystalline material with metastable phases [46], [69]–[71].

It should be noted that the crystallization model is only validated in the 160 – 168 °C temperature range and for nonisothermal cooling rates. The model assumes a two-phase system (amorphous and crystalline) with a maximum crystallinity limit of 30%, excluding different crystal phases.

Densification

The densification model in this study, describing particle coalescence and porosity reduction in SLS, is based on two distinct sub-models: one addressing viscoelastic sintering at higher porosities and another for bubble dissolution at lower porosities. Density ρ and porosity φ have a linear relationship

$$\rho = \rho_b \cdot (1 - \varphi) \tag{13}$$

and when porosity is equal to zero then density reaches its maximum value, the bulk density ρ_b 1.024 g cm^{-3} [70], [72]. Frenkel's sintering model, which assumes Newtonian

fluid mechanics, initially describes the viscous sintering of two particles with equal radius [73], [74]. However, polymer sintering involves both viscous and elastic forces [74], [75]. Given that a Newtonian model can overestimate early-stage coalescence rates in polymers, our model incorporates viscoelastic sintering based on the Upper-Convected Maxwell (UCM) model [74], [75]. This model assumes quasi-steady state flow and isothermal conditions for sintering between two particles [74], [75]. The primary viscoelastic sintering equation is given in Equation (14), with its components K_1 and K_2 defined in equations (15) and (16) [74].

$$8\left(\Lambda\tau K_1\frac{\mathrm{d}\theta}{\mathrm{d}t}\right)^2+\left(2\Lambda\tau K_1+\frac{\eta r_0 {K_1}^2}{\Gamma K_2}\right)\frac{\mathrm{d}\theta}{\mathrm{d}t}-1=0 \tag{14}$$

$$K_1=\frac{\sin(\theta)}{(1+\cos(\theta))(2-\cos(\theta))} \tag{15}$$

$$K_2=\frac{2^{-\frac{5}{3}}\cos(\theta)\sin(\theta)}{(1+\cos(\theta))^{\frac{4}{3}}(2-\cos(\theta))^{\frac{5}{3}}} \tag{16}$$

The Maxwell model constant Λ is set to -1 for viscoelastic sintering [74]. Stress relaxation time τ and viscosity η are temperature dependent. The value of surface tension Γ is taken as 34.3 mN m^{-1} [76], [77]. Surface tension Γ in Equation (14) is multiplied by the Farz Factor F to account for contact with additional particles, given that the original model was limited to two-particle interactions [78]. The initial particle radius r_0 is 30 µm, representing the median volume distribution diameter of DuraForm ProX PA powder [70]. Growth angle θ and its time derivative θ’ are derived using the quadratic formula and updated through the Explicit Euler method [12]. Stress relaxation time τ as a function of temperature is modeled in

$$\tau(T) = \tau_A \exp(\tau_B T) \tag{17}$$

fitting an exponential model to PA12 data with an R-squared value above 99% [77]. The pre-exponential factor τ_A is 12,107 s, and the exponential factor τ_B is -0.030124 K^{-1}. Zero-shear viscosity η is modeled as a function of temperature in

$$\eta(T) = \eta_{ref} \exp\left(-\frac{E_a}{R}\left(\frac{1}{T_{ref}} - \frac{1}{T}\right)\right) \tag{18}$$

using the Arrhenius equation [77]. Reference viscosity η_{ref} (9946 Pa s) and temperature T_{ref} (445 K) are based on DuraForm PA data, and the activation energy for viscosity E_a of PA12 is 55.2 kJ mol^{-1} [72], [77]. The Farz Factor F (which is multiplied with surface tension Γ in Equation (14)):

$$F = 1 + \frac{2}{3\sqrt{5}\cos(\theta)} \tag{19}$$

extends the viscoelastic sintering model from a two particle system to three particles to account for the effect of a neighboring particle [78]. The formulation of F in this work is derived from the original equation, which is dependent on particle radii and angle, with the assumption that the particles are of equal size, at a 90° angle, and with fixed relative positions. The growth angle θ is related to porosity φ through

$$\varphi = 1 - \frac{1-\varphi_0}{\left(1-\left(\frac{\sin(\theta)}{2}\right)^2\right)^3} \tag{20}$$

published by Scherer, modeling densification for a simple cubic lattice [79]. The initial porosity of the powder bed φ_0 is 0.58, calculated based on the tap density ρ_t of DuraForm PA, 0.43 g cm^{-3}, compared to the bulk density of Duraform ProX PA ρ_b [70], [72].

Scherer also notes that while sintering is the primary driver of densification above 6% porosity. Bubble dissolution, governed by Mackenzie and Shuttleworth's model (Equation (21)), becomes dominant below this threshold [79], [80]. The initial pore radius a_0 is assumed to match the initial particle radius r_0, and porosity φ is updated using the Explicit Euler method and the time derivative in Equation (21) when below 6%:

$$\frac{\mathrm{d}\varphi}{\mathrm{d}t} = -\frac{3\Gamma}{2\alpha_0\eta}\varphi \tag{21}$$

Molecular mobility is required for coalescence, with a critical absolute crystallinity value of 0.1 derived from literature observations, beyond which porosity remains unchanged [12]. In the model, porosity alterations are limited to the active layer, extending from the powder bed surface to a depth of one layer (100 µm).

Heat Equation

The thermal conductivity (λ) within our model is linked to the porosity of the material, as described by a linear rule of mixtures formula in Equation (22):

$$\lambda = \lambda_s(1-\varphi) + \lambda_g\varphi \tag{22}$$

This equation considers the thermal conductivities of both the solid material (λ_s) and the gas (λ_g) [72]. The gas component uses the thermal conductivity of nitrogen at specific conditions: 0.7 atm pressure and 200 °C temperature, which is 0.0375 W m^{-1} K^{-1} [81]. The thermal conductivity of the solid phase is derived from 3D Systems' data sheet for solid DuraForm ProX PA with a density of 0.95 g cm^{-3}, which reports a value of 0.21 W m^{-1} K^{-1} based on the ASTM E1530 standard [82]. This reported value corresponds to a material porosity of approximately 7.227%. Using this porosity and the provided thermal

conductivity values in Equation (22), the thermal conductivity of the pure solid (without porosity) is calculated to be 0.2234 W m^{-1} K^{-1}.

The model for the heat of melting/crystallization is adapted from existing literature, with modifications to make it functionally dependent on the crystallinity of the material [16], [83]. Equation (23) utilizes the rate of change in crystallinity to calculate the heat absorbed or released during the material's melting or crystallization process:

$$H_{\chi} = (1-\varphi) \cdot \rho \cdot \frac{d\chi}{dt} \cdot \Delta H_{100\%\ crystalline} \tag{23}$$

With these parameters established, the heat equation (24) is formulated as a transient energy balance:

$$\rho \cdot C_p \cdot \frac{\partial T}{\partial t} = \nabla(\lambda \nabla T) + \overline{q_{\ell}} + H_{\chi} \tag{24}$$

This equation accounts for time-dependent heat transfer elements on the left-hand side and Fourier's law of heat conduction on the right. Additional terms are incorporated to represent the effects of the laser and phase changes in the material. The heat equation is a core part of our thermal model, capturing the dynamic interplay between heat transfer, material properties, and phase transformations within the SLS process.

Numerical Implementation

The laser sintering process in our study is simulated using the Multiphysics Object Oriented Simulation Environment (MOOSE), a versatile parallel multiphysics finite element analysis framework [84], [85]. MOOSE was selected for its open-source

nature and extensive customization capabilities, allowing for seamless integration of various models within the simulation.

In the simulation, temperature is treated as a first-order Lagrange variable and is solved using the preconditioned Jacobian Free Newton Krylov method, complemented by automatic differentiation [86]. Porosity and crystallinity, key material properties, are calculated at each quadrature point using the Explicit Euler method. Initial conditions are uniformly set across the domain for temperature (173 °C), porosity (0.58), and crystallinity (0.45).

The simulation domain is configured as a rectangular prism, measuring 2 mm in both the x and y directions, with a height of 1.1 mm in the z direction. This domain is divided into active and inactive subdomains, with the initial active domain encompassing everything below a height of 0.4 mm. Variables change only within this active domain, while the inactive domain reserves space for the addition of new layers during the simulation. The domain is discretized with a mesh of cubic Hex8 elements, each with a side length of 20 µm. This mesh size strikes a balance between detail and computational efficiency, as confirmed by negligible differences in results between 50 µm and 20 µm simulations. As new 100 µm layers are added, they are subdivided into 20 µm increments across several time steps.

On the boundary between active and inactive domains, a convective heat transfer boundary condition is applied as per Equation (25):

$$q_c = h\left(T - T_a\right) \tag{25}$$

with a convective heat transfer coefficient h of 15 W m^{-2} K^{-1} [53]. The ambient temperature T_a is initially set at 173 °C. The other sides of the active domain have Dirichlet boundary conditions, maintaining constant temperatures equal to T_a. After the laser scans, the model dynamically recalculates temperature-dependent properties, resolves melting/crystallization, decreases porosity (if crystallinity is below 10%), and updates density for the subsequent time step.

A CSV file inputs data for time stepping, laser positioning, layer deposition, and cooling. The time steps are defined to emulate a laser velocity of 12.7 m s^{-1}. When the laser is inactive, and the material is cooling, the time step size incrementally increases. The laser scans a 1 mm area in the domain center, alternating direction with each of the six layers.

Without termination criteria, the densification model is unbounded, and porosity will continue to decrease as time passes. To calibrate the model, simulations were performed with a range of laser powers, and densification proceeded for 30 seconds. Figure 13 shows that, except for 31 W, simulated porosity values closely match experimental ones at 12 seconds. Therefore, a 12 second interval is used in multilayer simulations between layer scanning. After the final layer is scanned and 12 seconds pass, the ambient temperature for boundary conditions is reduced to 135 °C. The porosity and

crystallinity of each element are recorded at each time step for analysis.

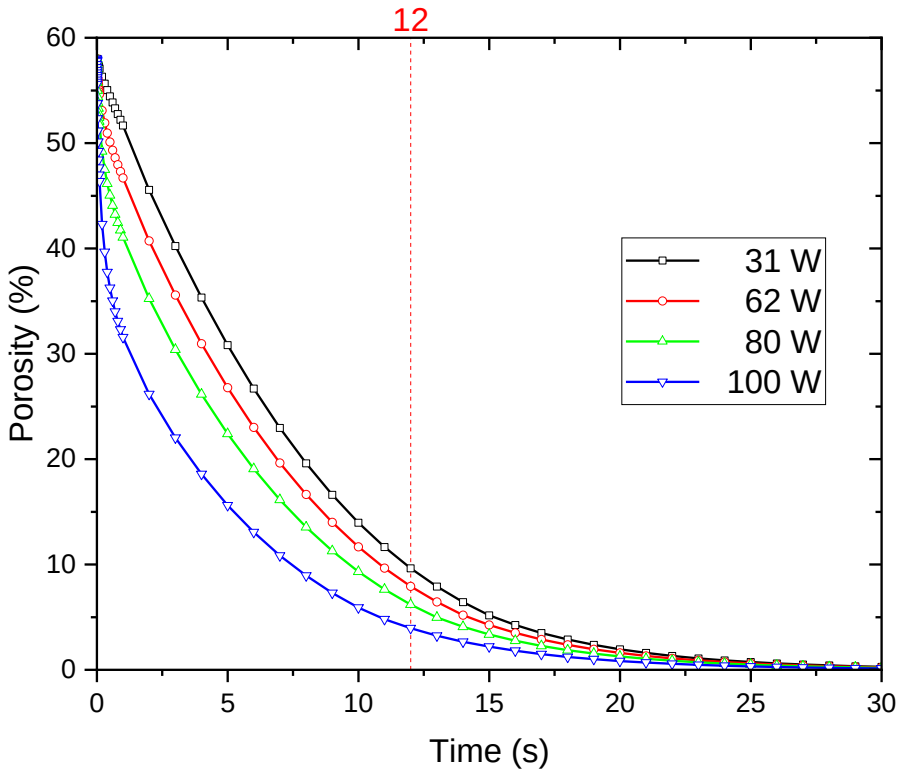

Figure 13. Porosity tracking over time for a single 1 mm square layer scanned at different laser powers, showing simulated values closely matching experimental ones at 12 seconds, except for 31 W.

This comprehensive approach to finite element analysis allows for simulation of the laser sintering process, capturing the intricacies of temperature variations, material properties, and layer deposition in a highly controlled and predictive manner.

Results and Discussion

Multilayer process simulations were conducted using various laser powers to assess the impact on final porosity. To analyze the final porosity output, porosity values were extracted from a vertical column (z-column) at the domain's central x and y axes. A specific 0.4 mm segment of this z-column was selected, excluding the top and bottom layers to mitigate boundary effect-induced inconsistencies.

In Figure 14, the porosity patterns observed through both Micro-CT and simulation are plotted against different laser powers. The X-axis represents the relative Z-height within the sample.

For the Micro-CT results in Figure 14(a), all laser power settings exhibit a consistent periodic variation in porosity, with a period corresponding to the 0.1 mm layer height used in specimen printing. Lower laser power is associated with higher average porosity and more pronounced periodic variation amplitudes. In the simulation results in Figure 14(b), the lowest porosity (troughs) consistently appears at the top of each layer, where the laser imparts the most heat. Conversely, porosity peaks are observed at the points within each layer that are furthest from the top. Additionally, the oscillations of porosity in the z-direction from the simulation have several differences compared to experimental observations. For the simulation’s oscillations, the magnitudes are lower, they never overlap between laser powers, and the signals are much less noisy. This may be caused by the homogeneous material properties in the simulation in contrast to the randomly packed distribution of powder particles present in real systems.

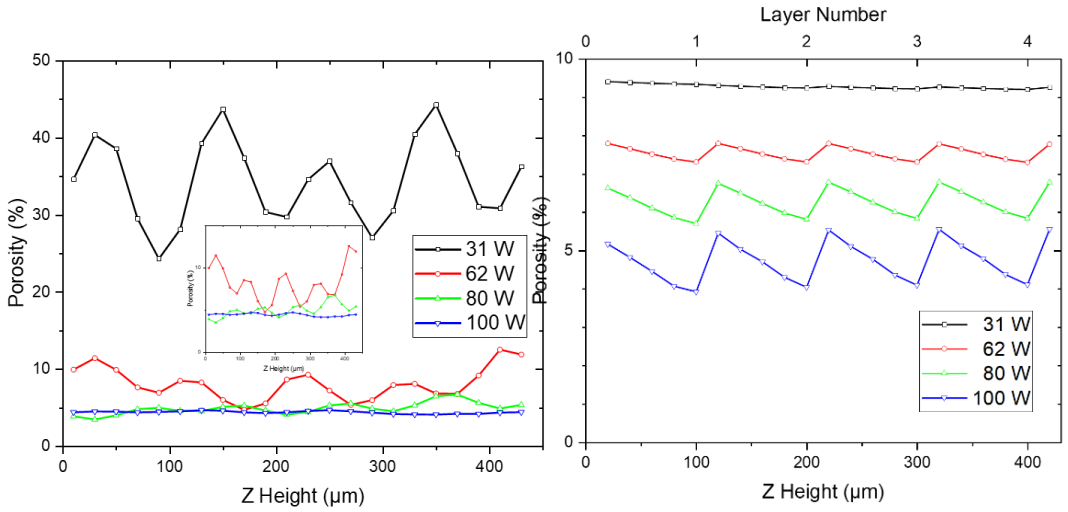

(a) (b)

Figure 14. a) Porosity through the Z height of coupons produced at different laser powers as measured by Micro-CT. b) Simulated porosity through the Z height of the domain for different laser powers.

The average porosity values of these simulated 0.4 mm segments are plotted with experimental measurements against different laser powers in Figure 15. These simulated segments also form the basis for the RVEs in the mechanical model. The results are summarized in Table 7. Additional data for density measurements are available in Appendix B.

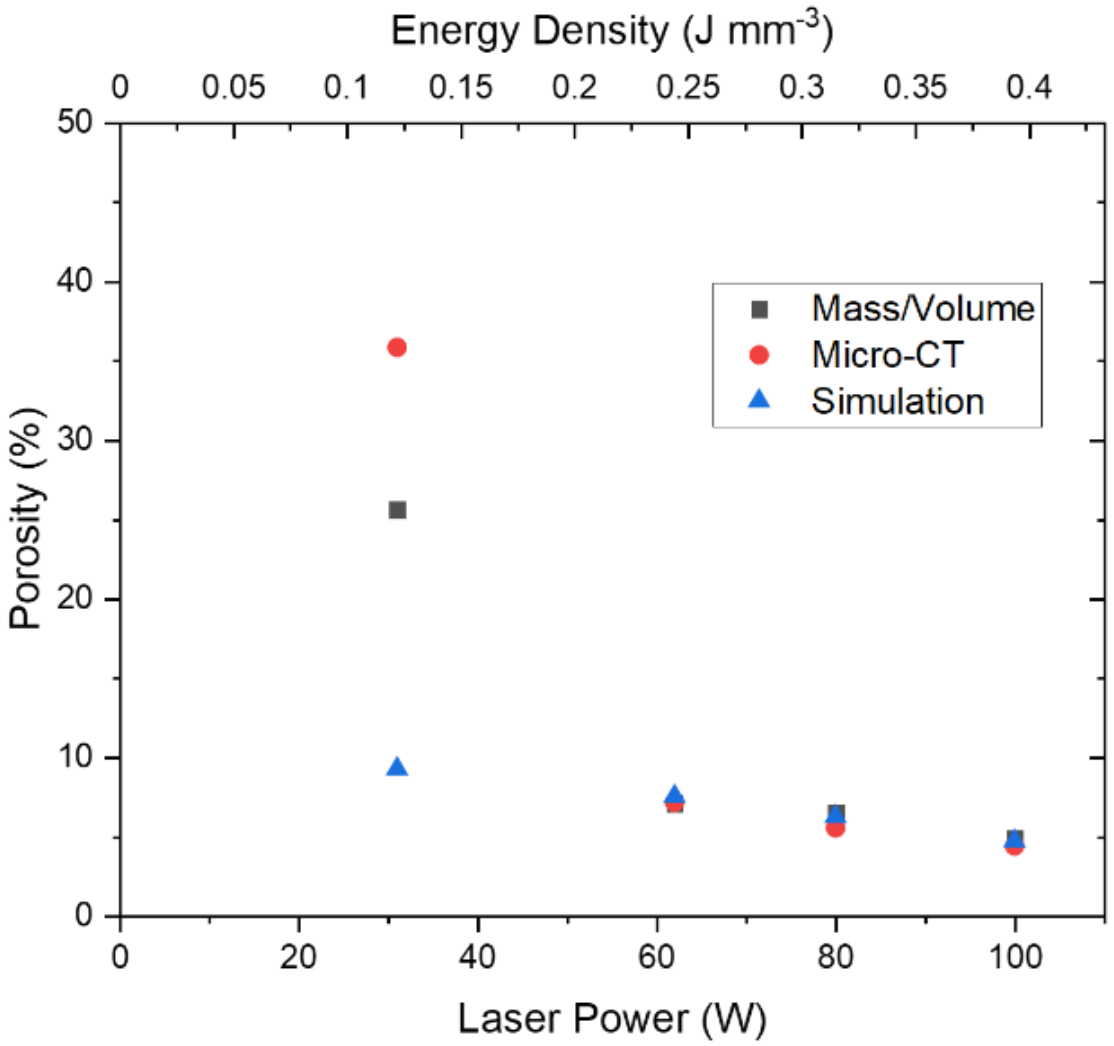

Figure 15. Porosity comparison between experimental measurements and simulation for different laser powers.

Table 7. Summary of experimental and numerical results.

Laser Power (W)	E_v (J mm^{-3})	Crystallinity (%)	Mass/Volume Porosity (%)	Micro-CT Porosity (%)	Simulation Porosity (%)
31	0.122	31.7	25.60	35.86	9.28
62	0.244	30.6	7.11	7.17	7.55

80	0.315	29.6	6.48	5.56	6.27
100	0.394	29.2	4.88	4.43	4.73

As shown in Figure 15, the experimental porosity of specimens decreases monotonically with increasing laser power. A significant reduction in porosity is observed when comparing 31 W to 62 W, with diminishing returns beyond 62 W.

Differences between mass/volume and Micro-CT measured porosity arise because only the fill scan laser power was altered during specimen printing, leaving the outline scan unchanged. Micro-CT analysis excludes outer specimen regions affected by the outline scan, leading to discrepancies compared to mass/volume measurements, encompassing these areas. Since the outline scan parameters are optimized for 62 W fill scans, inner porosity (better captured by Micro-CT) is higher than overall porosity from mass/volume at fill powers below 62 W and vice versa for powers above 62 W.

The average porosity predicted by simulations aligns closely with experimental data at 62 W and higher but diverges at 31 W. The cause of this divergence is unclear, but it may stem from factors such as partial melting, nonisothermal conditions, and the effects of crystallization on fluid properties, which are not fully considered in the model [77]. The time-based termination criterion is less effective for 31 W than the other laser powers.

The model's limitations include its reliance on property data from various grades of PA12 powder, condensation of powder property distributions into singular values, simplifications in fluid dynamics, a time-based termination criterion for densification,

generalizations of thermal history, and a simplified representation of phases. Future models may benefit from:

- More comprehensive material characterization
- Discrete powder particles with a distribution of properties
- Explicit modeling of fluid dynamics
- A more advanced understanding of the termination criteria that govern densification
- Extended and varied thermal histories
- The modeling of multiple crystal phases

Despite this, the model shows good agreement with experimental data in low porosity scenarios, typical of near-complete melting conditions in SLS.

Conclusion

Integrating phase transformation, densification, and heat transfer, the process model is adept at predicting the microstructural evolution from powder to solid. This bottom-up approach to modeling process-structure-property-performance relationships enables the prediction of material properties and performance, and would allow for a top-down approach that tailors the process parameters to induce a desired material structure, like in [7].

However, it's important to acknowledge certain limitations. The model does not fully encapsulate the thermal history of parts produced in SLS, particularly regarding part

placement within the print bed. Furthermore, the simulated domain is a simplified representation of the more complex, large-scale manufacturing process.

The crystallization model, while effective, is confined to isothermal conditions and a narrow temperature range just below the melting point of PA12. The densification model, based on an idealized sintering concept, assumes spherical, identical particles and isothermal conditions. To enhance its applicability, the model requires extensions to incorporate the dynamics of multiple particle contacts and varying packing configurations. The effects of lower laser power are not accurately captured by the model, and future work is planned to improve upon this aspect.

CHAPTER THREE

THERMAL DEGRADATION IN THE MELT POOL

Task 2 requires gathering experimental data for degradation of PA12 in conditions like SLS and creating a reaction model that integrates into the process model. The reaction model uses the temperature from the process model to predict the amount of mass lost as water from post-condensation. The mass loss affects the process model by modifying the density of the material, which may have effects on the thermal diffusivity and cooling rates of the material. The simulations include a range of laser powers to explore the relationship between energy density and degradation.

Materials and Methods

Thermogravimetric Analysis (TGA)

The Ozawa/Flynn/Wall method (as detailed in ASTM E1641) was used to determine activation energy of post-condensation through thermogravimetric analysis with a TGA5500 (TA Instruments) [87], [88]. Powder samples weighing 3±1 mg were placed in a platinum high temperature pan and heated at rates of 4, 6, 8, and 10 °C/min in a nitrogen atmosphere. DuraForm ProX PA powder with a 40% refresh rate was used in this study.

Modeling

The post-condensation reaction follows the general form in Equation (26) where C represents one of the products, such as H_2O.

$$A + B \rightarrow C + D \tag{26}$$

With first order kinetics, the rate of generation of product C can be represented as:

$$\frac{dC}{dt} = A_C(1-C)\exp(-\frac{E_C}{RT}) \quad (27)$$

Equation (27) is implemented in MATLAB and MOOSE using the explicit Euler method and kinetic parameters determined from TGA. In MOOSE, the degradation model is integrated into the process model described in Chapter Two, and mass loss from the chemical reaction has a direct effect on density.

Results and Discussion

Experimental

Similar to other works, the experimental results were rescaled to eliminate the effect of water evaporation on mass loss – the graphs start at 100 °C and the mass is rescaled to 100% at that temperature [11]. These data for each heating rate are plotted in Figure 16 and the points of 5% mass loss are determined.

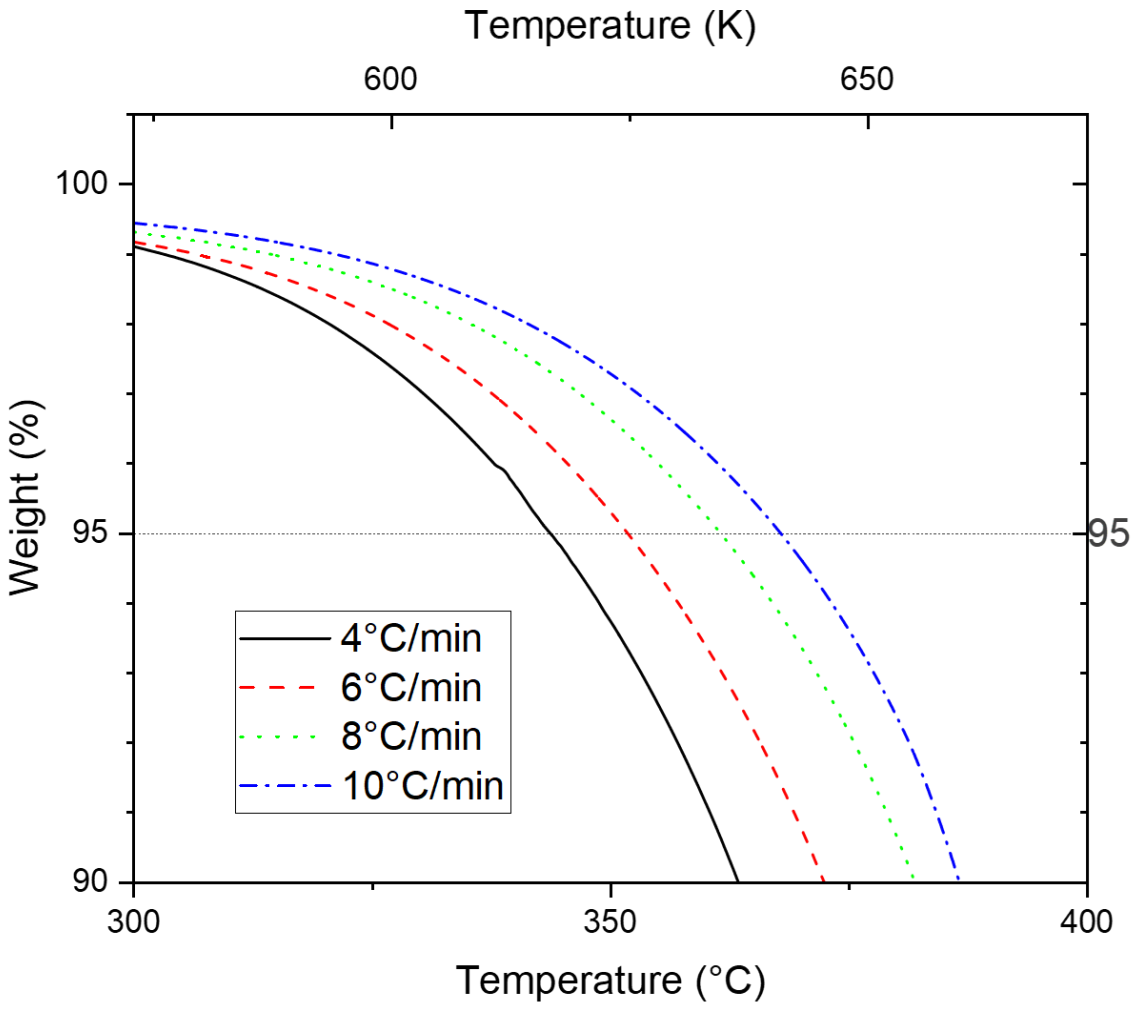

Figure 16: Points of 5% mass loss for PA12 powder heated at different rates.

The inverse temperature of 5% mass loss is linearized against the logarithm of the heating rate in Figure 17. This enables the determination of the activation energy and the pre-exponential factor.

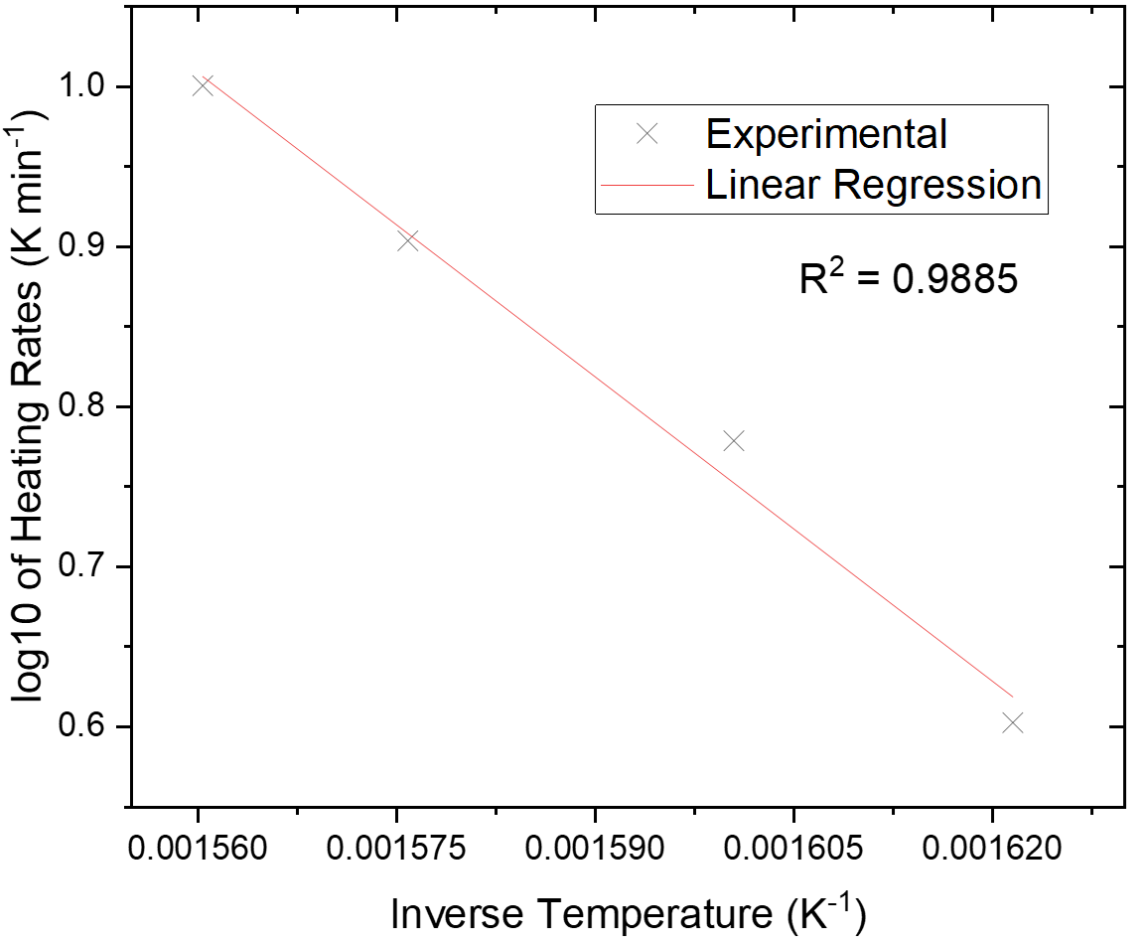

Figure 17: Linearization of temperatures of 5% mass loss with heating rates.

The activation energy of the reaction is estimated by the slope of a line fit to the data in Figure 17. This estimate is improved through an iterative method explained in ASTM E1641 to yield the activation energy (110.8 kJ mol^{-1}) and pre-exponential factor (1.96 min^{-1}) for the reaction. The activation energy is on the same order of magnitude as other investigations of PA12 degradation, but as observed firsthand and noted in other works, the activation energy is dependent on the degree of mass loss chosen to calculate it [11], [89]. If 1% or 10% mass loss had been chosen as the criterion instead, the

activation energy would differ. However, kinetic parameters calculated with 1% and 10% mass loss did not match experimental results as well as 5%.

Numerical

Utilizing the reaction model with kinetic parameters defined in the preceding section, numerical experiment was conducted to benchmark the model against experimental observations at a heating rate of 8 °C/min. This comparison utilized MATLAB and MOOSE for model implementation, with conditions aligned to replicate the experimental time-temperature profile. The numerical outcomes from both software implementations exhibited a high degree of congruence with the experimental data, particularly within the initial 10% of mass loss, indicating negligible discrepancies between the two modeling approaches (Figure 18).

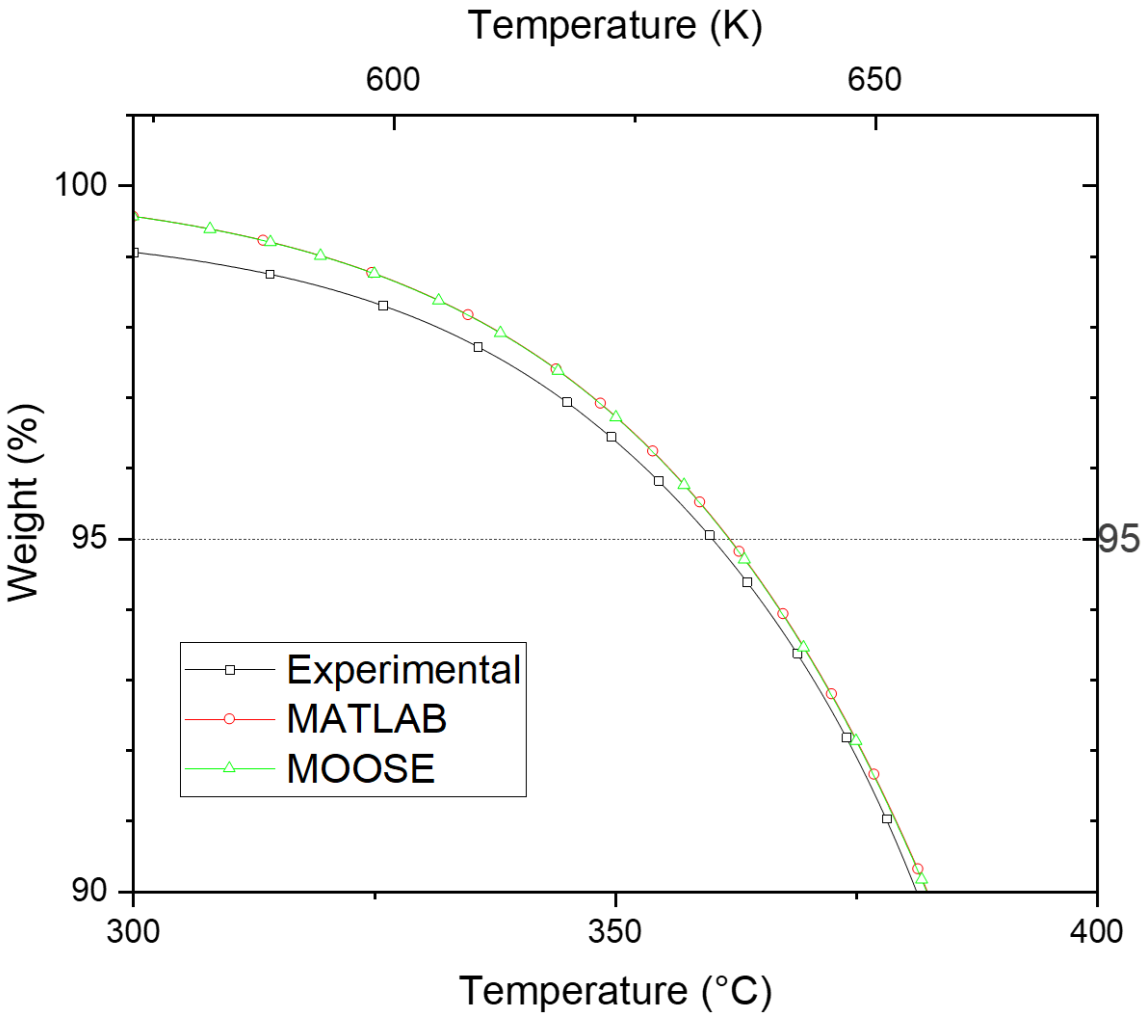

Figure 18: Validation of the reaction model through comparison to experimental data for 8 °C/min heating rate.

In an advanced simulation incorporating the process model introduced in Chapter Two, a 1 mm square area underwent scanning with subsequent convection cooling, during which maximum temperature and mass loss were recorded. This simulation was executed across laser powers ranging from 62 W, deemed “optimal,” up to 200 W. The corresponding results, depicted in Figure 19, illustrate the temperature dynamics and

mass loss over both linear and logarithmic time frames for melt pools subjected to varying laser powers.

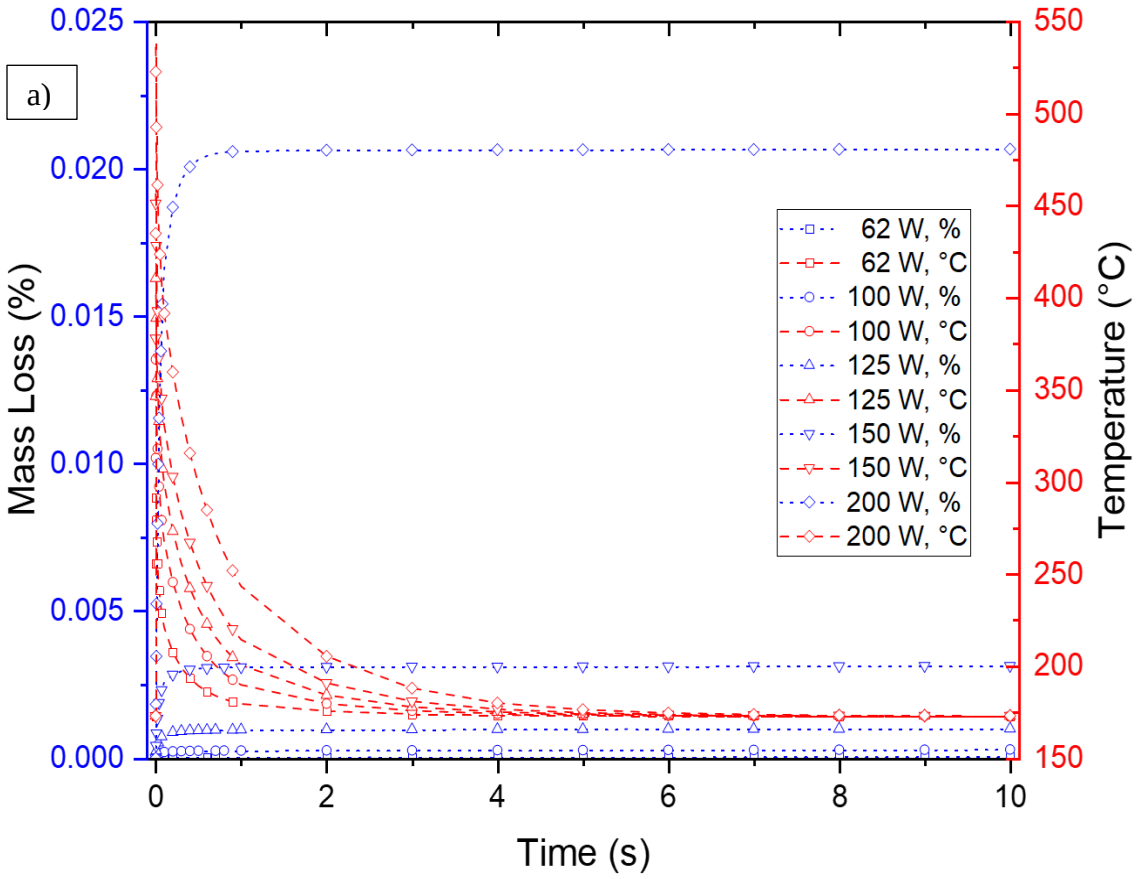

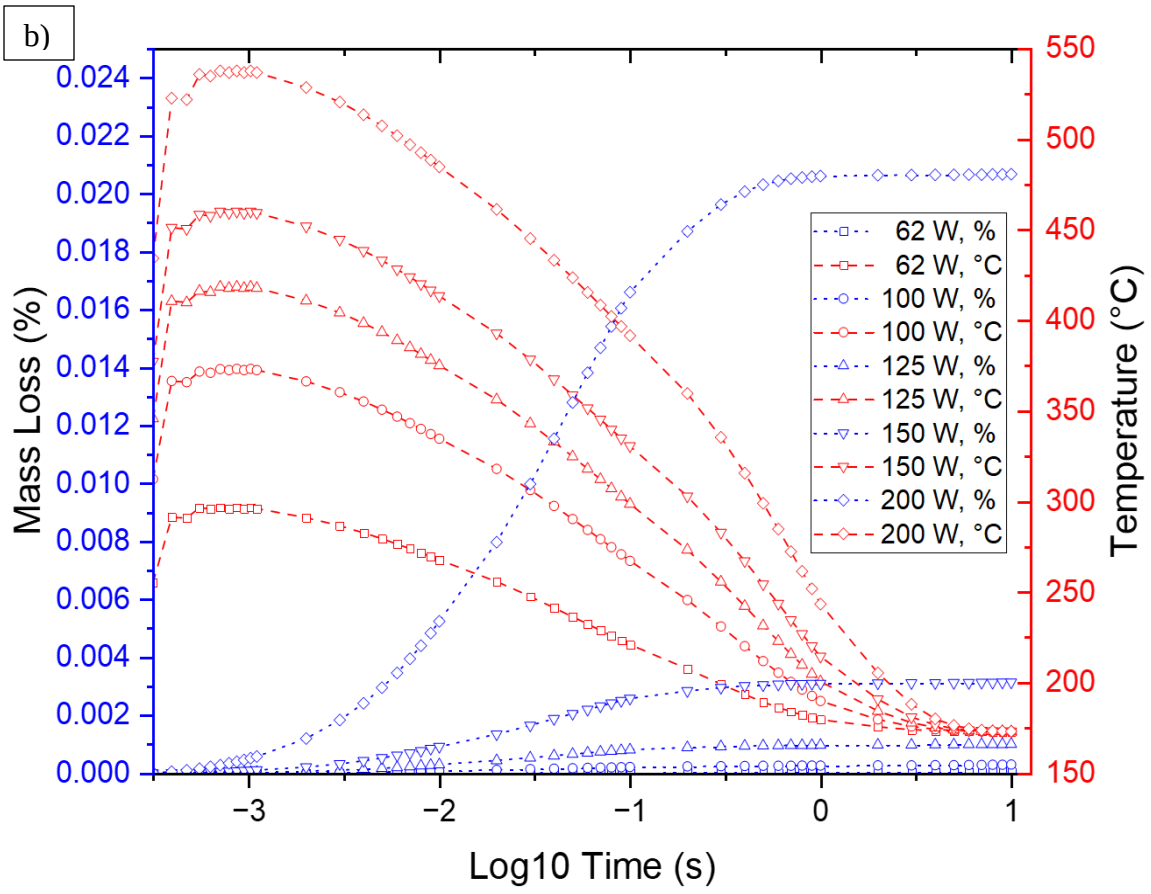

Figure 19. Temperature and mass loss over a) linear time and b) logarithmic time for melt pools at different laser powers.

The temperature peaks observed immediately post-laser scan swiftly diminish, approaching a baseline of 173 °C within a few seconds. Notably, the bulk of the degradation, as evidenced by mass loss, transpires within the first second amidst peak temperature conditions, with a gradual and linear progression of degradation thereafter as temperatures plateau.

Escalating the laser power from 62 W to 125 W incurs a modest uptick in degradation; however, further elevation to 150 W and 200 W markedly amplifies degradation levels. Despite predictions that processing temperatures exceeding 320 °C

would foster degradation [21], these findings indicate that the maximal percent mass loss is around 0.025% with a laser power of 200 W, demonstrating that mass loss exerts a minimal impact on material density relative to other processes like sintering. Consequently, this mass loss imparts an insubstantial effect on the thermal attributes of the material, leaving melt pool temperatures largely unaffected.

Conclusion

The integration of the reaction model into the process model predicts minimal post-condensation during laser sintering, even under the highest laser powers evaluated. The quantified mass loss is minimal, with no pronounced influence on melt pool temperature dynamics. While the model's current rendition offers valuable insights, there is room for enhancement through the inclusion of additional chemical reactions such as oxidation, chain scission, or pyrolysis, which could provide a more comprehensive understanding of thermal degradation phenomena [23], [90]. The model's parameters are calibrated based on degradation data proximal to 350 °C, thus the fidelity of the model's predictions at elevated temperatures remains to be fully validated.

Future work could improve these models by integrating a broader spectrum of chemical reactions and extending the validation range to encompass higher temperature domains. Such advancements will not only bolster the model's accuracy but also enhance our ability to predict and mitigate thermal degradation in SLS, thereby improving the quality and reliability of manufactured parts.

CHAPTER FOUR

EXPANDING THE PROCESSING WINDOW WITH LASER BEAM PROFILES

In Task 3, laser beam profiles other than the Gaussian distribution are implemented into the process model. Process simulations are performed with each laser beam profile to analyze how the beams affect melt pool characteristics, processing windows, and microstructural outcomes. Due to a plethora of parameters, the design space is untenably large, thus the laser beam profiles tested in this study all have the same nominal radii and total power. This eliminates the elliptical beam from this analysis, as the focus area inherently differs from the Gaussian, top-hat, ring, and Bessel beams. Scan velocity is kept constant, however a range of scan spacings are explored. Material properties are the same as those detailed in Chapter Two. The resulting temperature profiles, maximum temperatures, and porosity profiles provide valuable information about the effects of the laser beams.

Methods

Intensity Distributions

Equation (28) describes the combination of a 2D Gaussian distribution with the Beer-Lambert law perpendicular to it in Figure 20a, providing the heat imparted by the laser into the substrate as a function of x, y, and z coordinates [56]. Here, A is absorptivity, β is the extinction coefficient, P is laser power, r_G is the radius of laser ($1/e^2$ of peak intensity), and x_t, y_t, and z_t are the coordinates that the laser is centered on at time t.

$$Q_G = \frac{2A\beta P}{\pi {r_G}^2} \exp\left(-\frac{2}{{r_G}^2}\left(\left(x - x_t\right)^2 + \left(y - y_t\right)^2 \right) + \beta(z - z_t) \right) \tag{28}$$

The top-hat beam in Figure 20b is described in Equation (29) using the rectangular function which is equal to 1 if the value is between $-r_T$ and r_T, and equal to 0 elsewhere [56].

$$Q_T = \frac{A\beta P}{\pi {r_T}^2} rect\left(\sqrt{(x - x_t)^2 + (y - y_t)^2} \right) \exp\left(\beta(z - z_t) \right) \tag{29}$$

The ring beam in Figure 20c can be produced with Equation (30) where r_r is the radius from the center to the middle of the ring and r_b is the radius ($1/e^2$ of peak intensity) of the ring [44].

$$Q_R = \frac{2A\beta P}{\pi {r_b}^2 Y} \exp\left(-2\left(\frac{\sqrt{(x - x_t)^2 + (y - y_t)^2} - r_r}{r_b} \right)^2 + \beta(z - z_t) \right) \tag{30}$$

The term Y is defined in Equation (31) [44].

$$Y = \exp\left(-2\left(\frac{r_r}{r_b} \right)^2 \right) + \frac{\sqrt{2\pi} r_r}{r_b} erfc\left(-\frac{\sqrt{2} r_r}{r_b} \right) \tag{31}$$

A Bessel beam (Figure 20d) is produced by combining the Gaussian beam and the ring beam in Equation (32) with term f_P to split the power between each component [44].

$$Q_B = f_P Q_G + (1 - f_P) Q_R \tag{32}$$

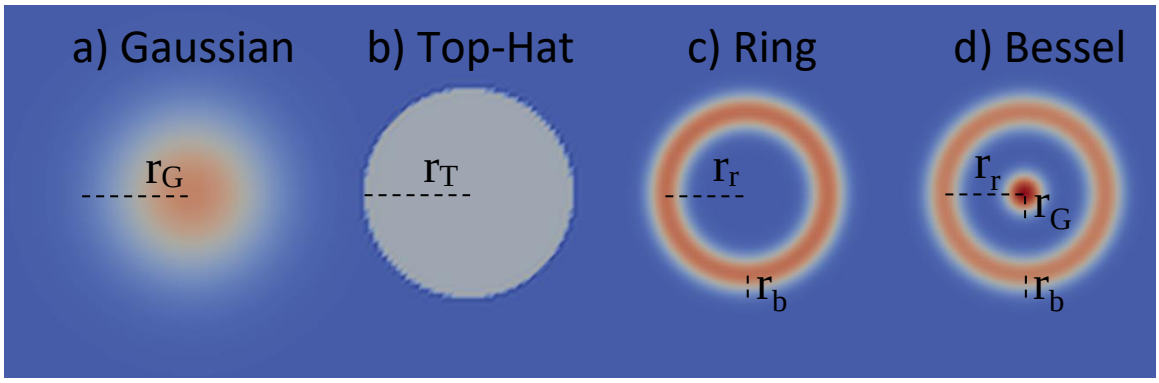

Figure 20. Demonstration of intensity profiles and radii for a) Gaussian, b) top-hat, c) ring, and d) Bessel beams [44].

Simulation Conditions

In numerical simulations, the laser power is set to 62 W and the scan speed to 12.7 m s^{-1}. Material properties and initial conditions are the same as the model discussed in Chapter 2. The absorptivity is set to 0.94 and the extinction coefficient to 9000 m^{-1} (informed by experiments for PA12 powder) [53], [57].

The radius of the Gaussian and top-hat beams is 225 µm. For the ring and Bessel beams, r_r is 175 µm and r_b is 50 µm. Additionally for the Bessel beam, the radius of the Gaussian component is 50 µm and the power split f_P is 0.1. These radii were chosen so that the focus area for all beams is 225 µm. The power split f_P of the Bessel beam was iteratively tested and 0.1 was determined to provide nearly identical maximum temperatures in the Gaussian and ring components in single scan simulations.

To compare the effects of the intensity distributions, a single scan of 1 mm is simulated with each of them while keeping other conditions the same. These simulations were performed in a 2 * 1 * 0.5 mm domain with a 20 µm mesh. Nodes perpendicular to the scanning direction have their temperature tracked and recorded at 0.1 ms, after the

laser scan is complete. Surface elements perpendicular to the scanning direction have their porosity tracked and recorded at 12 s once sintering is complete.

A second set of simulations were performed in which 1 mm long scans were applied parallel to each other for each intensity distribution and with variable scan spacing. The domain is 2 * 2 * 0.5 mm with a mesh size of 50 µm. Temperature was tracked perpendicular to the scanning direction and recorded at 1 ms. Surface porosity perpendicular to scanning was recorded at 12 s.

Results and Discussion

Single Scans

The surface temperature after a single scan with each laser type is captured in Figure 21, with a profile through the center in the y-direction extracted for Figure 22 and the maximum temperatures summarized in Table 8. The Gaussian beam in Figure 21a produces a Gaussian temperature profile with the steepest decline of the set in Figure 22, reaching close to ambient temperature at about 180 µm away from the center. The top-hat beam in Figure 21b results in a flatter temperature profile, declining to ambient temperature at about 220 µm. The top-hat distributes heat more evenly than the Gaussian beam, giving it a maximum temperature about 20 °C lower than Gaussian. However, this distribution is not completely flat due to the overlapping effect of the laser beam in the x-direction as it scans across the domain along that axis. In Figure 21b, the area in the center of the top-hat has a higher temperature than the edges in the y-direction because the length in the x-direction across the circle at its center is at a maximum. In the center

of the ring beam is the lowest temperature of all the beams due to a minimal amount of overlapping. The ring beam has the highest maximum temperature of all the beams, occurring in the outer region at about 175 µm where it overlaps itself most intensely. The Bessel beam shares characteristics of the Gaussian and ring beams, showing temperature peaks in the center and at 175 µm. Its maximum temperature is lower than both the Gaussian and ring beams, but higher than the top-hat beam. The top-hat, ring, and Bessel beams decline to ambient temperature at about the same distance of 220 µm, greater than the Gaussian beam, by radiating heat more evenly throughout the focus area.

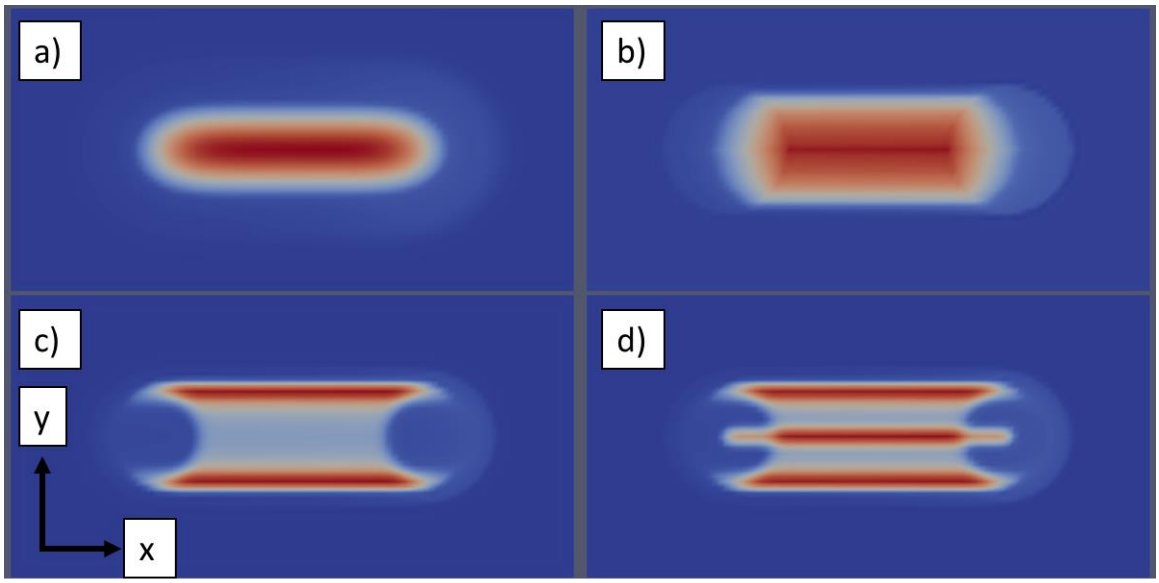

Figure 21. Surface temperature from single scans using a) Gaussian, b) top-hat, c) ring, and d) Bessel beams.

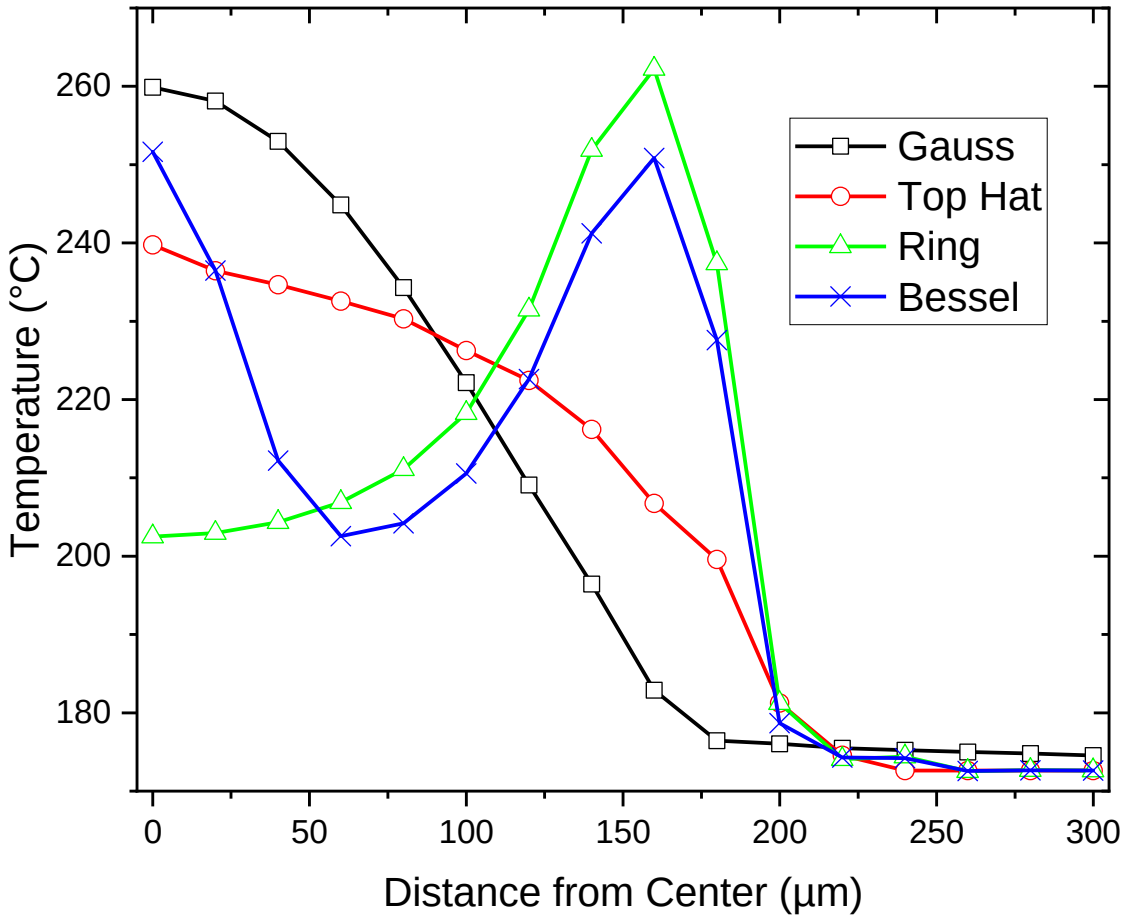

Figure 22. Surface temperature profiles at 0.1 ms, after the 1 mm laser scan is complete.

Table 8. Maximum temperatures at 0.1 ms for each intensity distribution resulting from a 1 mm scan.

LASER TYPE	MAX TEMPERATURE [°C]
GAUSS	259.9873
TOP-HAT	240.5042
RING	262.7701
BESSEL	252.1023

In Figure 23a, the porosity profiles for all the beams appear equal except for the point that they transition to 58% which represents unsintered powder. Gaussian is the first to reach this threshold, followed by top-hat, then Bessel, and finally the ring beam. Powder on the outer periphery remains unsintered due to insufficient melting which is directly related to the temperature profile. Melt pool radius data is summarized in Table 9. Because Gaussian had the steepest temperature decline, it has the lowest melt pool radius. This is followed by the top-hat which spreads heat more widely than the Gaussian beam, but because the temperature decreases at an earlier point than the ring and Bessel beams, its melt pool radius is lower than theirs. Figure 23b focuses on the melt pool region and shows the subtle differences between the porosity profiles at this scale. Although the magnitude of these differences is small, they show that the ring beam results in the flattest porosity profile followed by the Bessel, top-hat, and Gaussian beams. This is related to the temperature profiles of Figure 22, but also influenced by the heat diffusion that follows the laser scans. Sintering is a time and temperature dependent phenomenon, and the spreading of heat after a laser scan is important in the process. Therefore, while the ring beam has a temperature profile with a low temperature in the center at 0.1 ms, as time passes the temperature profile becomes flatter, manifesting in the porosity profile. While the Bessel beam has a nearly equal temperature in the center and periphery at 0.1 ms, the concentration of heat in the center ultimately causes a lower porosity in the center at 12 s.

Table 9. Melt pool radius for each intensity distribution after a 1 mm laser scan.

LASER TYPE	**MELT POOL RADIUS [μm]**

GAUSS	160
TOP-HAT	180
RING	200
BESSEL	200

a)

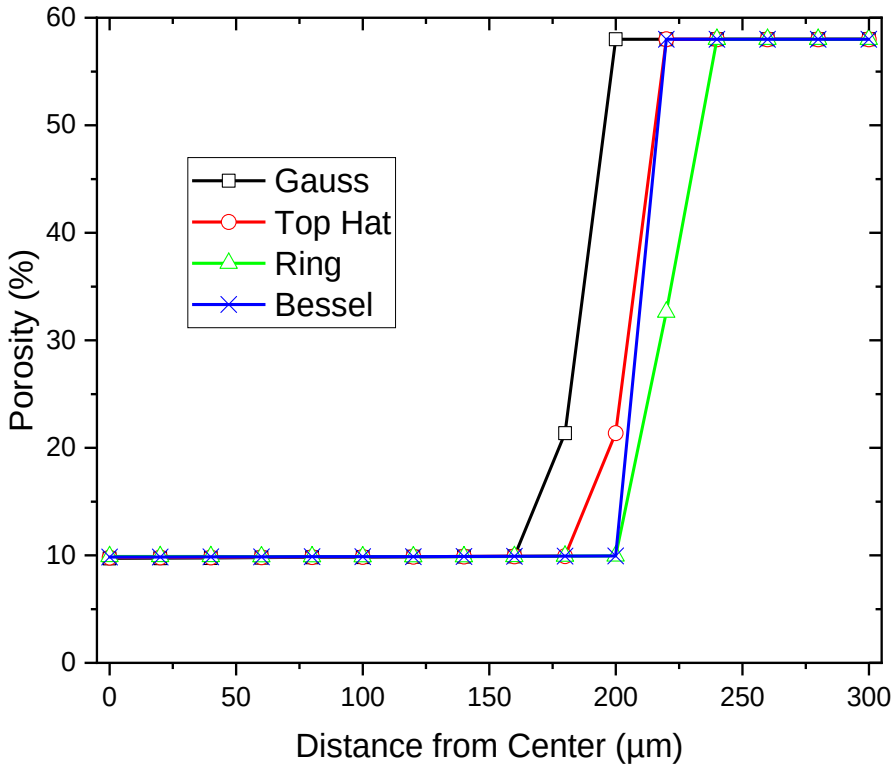

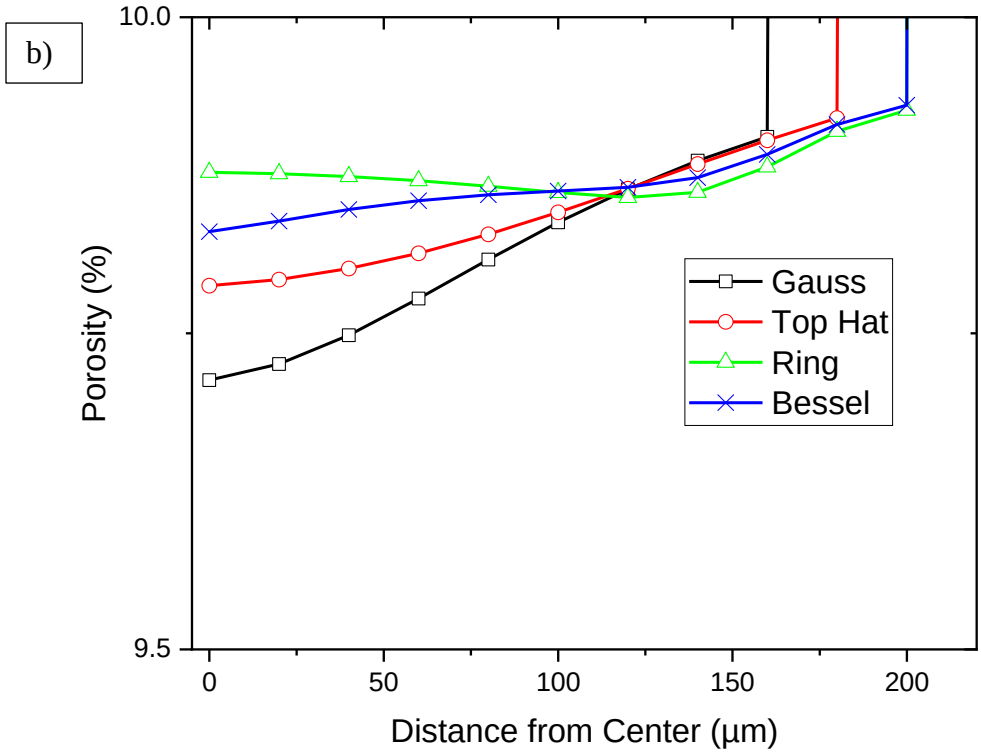

Figure 23. a) Surface porosity profiles at 12 s with b) a focus on the melt pools for a 1 mm laser scan.

Parallel Scans

In Figure 24, the surface temperature from parallel scans 200 µm apart shows distinct patterns for each laser type. Because the laser has a radius of 225 µm and the scan spacing is less than double this radius, there are regions of overlap between parallel scans. Figure 25 shows temperature profiles for scan spacings of a) 200 µm (manufacturer recommended value) and b) 250 µm.

The Gaussian beam with 200 µm scan spacing in Figure 24a and Figure 25a results in a very uniform temperature distribution and the flattest temperature profile of

the set despite having a steep temperature gradient in Figure 22. Overlapping is advantageous to temperature uniformity for the Gaussian beam.

For the other laser types, overlap results in temperature maxima and minima between the scans. The top-hat beam, intended to provide a flat temperature profile in the substrate, results in a periodic temperature profile due to overlapping in Figure 24b and Figure 25. The regions with the highest temperature have a triple overlap between adjacent scans.

The ring beam in Figure 24c and Figure 25a has greater temperature fluctuations than the top-hat beam due to overlapping rings which have more concentrated energy than the top-hat.

In Figure 24d and Figure 25a, the Bessel beam has the highest temperature due to overlapping of the ring component and Gaussian component between adjacent scans, while this does not occur for a scan spacing of 250 μm.

In Figure 25b with a scan spacing of 250 μm, the ring beam has the highest temperature due to overlapping of its ring between adjacent scans. In Figure 25b, the Gaussian beam's temperature profile begins to take a periodic shape as the scan spacing becomes large enough to lead to uneven heat application. The location and degree of overlapping is dependent on laser intensity distribution as well as scan spacing.

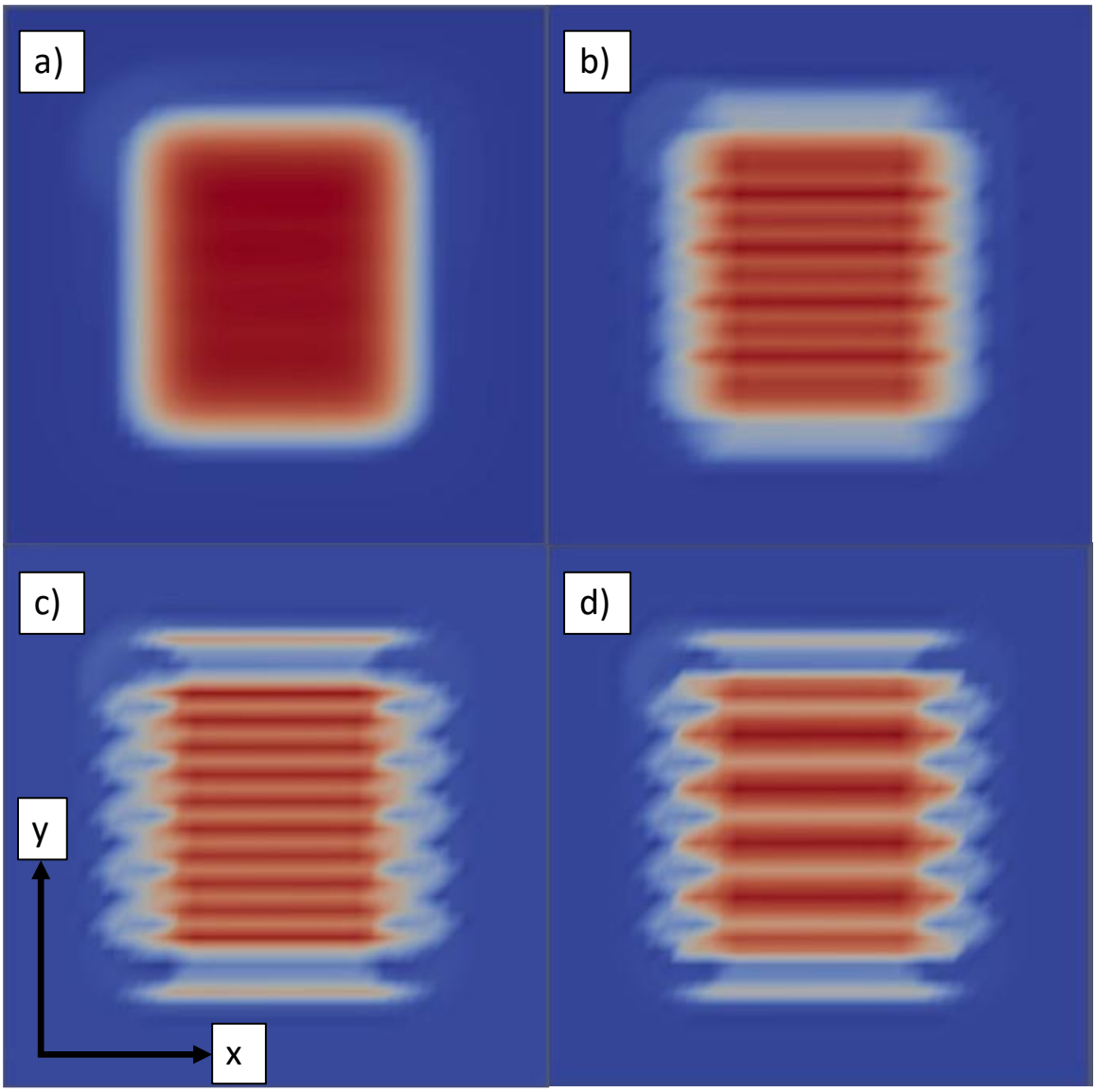

Figure 24. Surface temperature from parallel scans 200 µm apart using a) Gaussian, b) top-hat, c) ring, and d) Bessel beams.

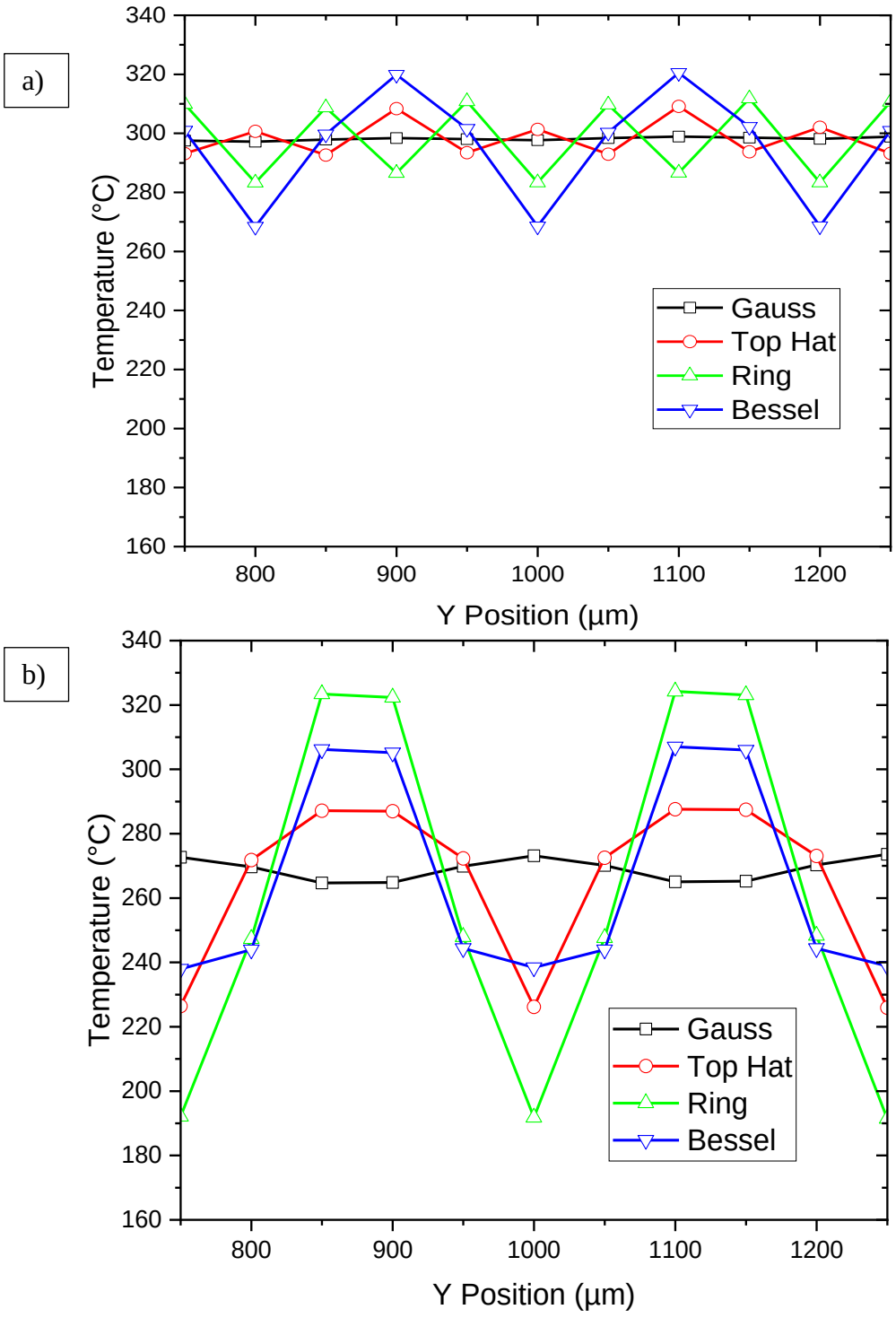

Figure 25. Surface temperature profiles for parallel scans with scan spacings of a) 200 µm and b) 250 µm.

Figure 26 shows the porosity profiles associated with the temperature profiles in Figure 25. With a scan spacing of 200 μm in Figure 26a, the top hat, Gaussian, and ring beams provide similarly flat porosity profiles with increasing porosity between each laser type. The temperature profile induced by these lasers has low enough fluctuations that there are no discernible fluctuations in porosity. However, the temperature fluctuations induced by the Bessel beam result in noticeable fluctuations in porosity, unlike the other laser beams in Figure 26a. With a greater scan spacing in Figure 26b, all laser beams induce periodic variations in porosity corresponding to the scan spacing because heat is not distributed evenly. Greater scan spacing reduces energy density, resulting in higher porosity.

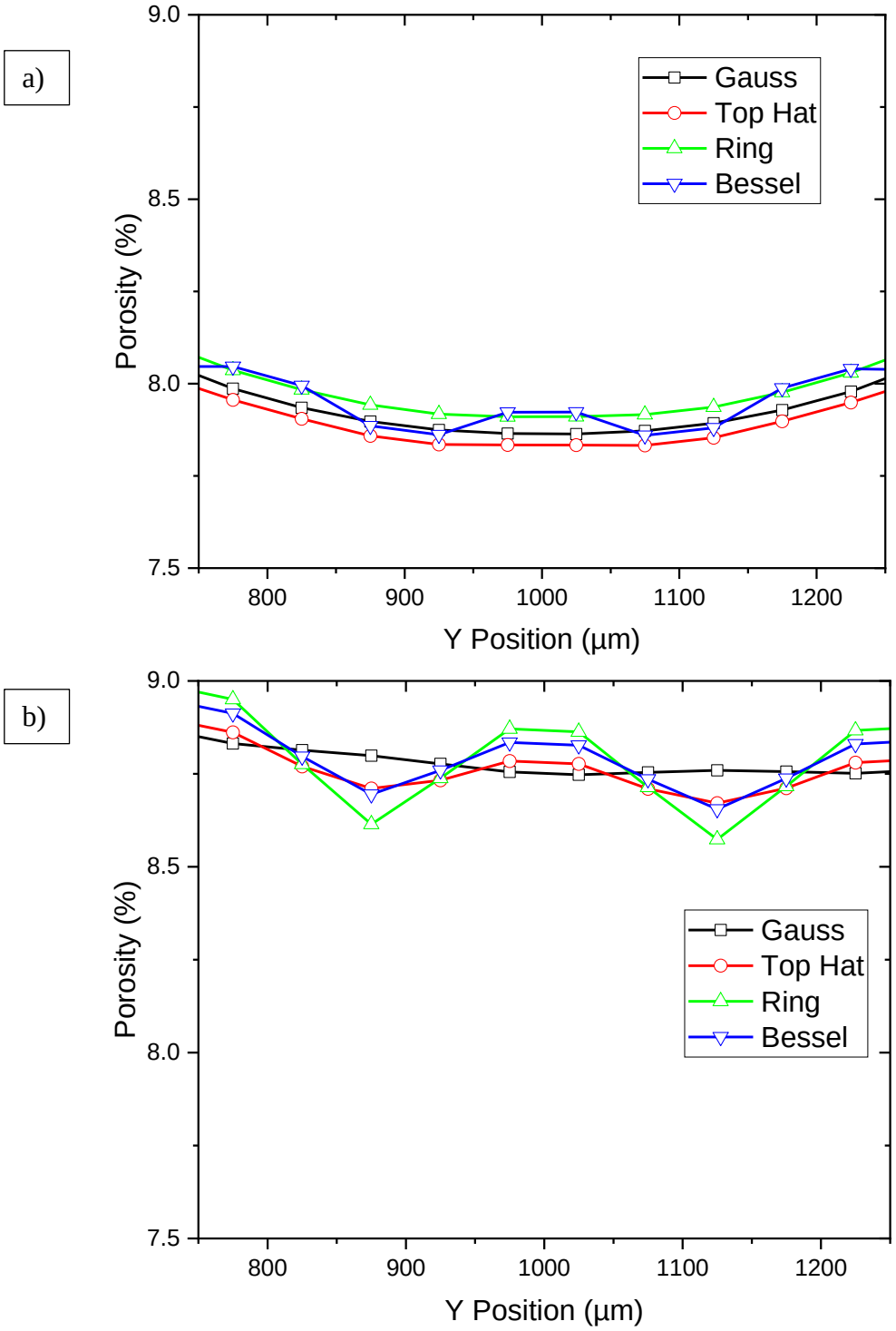

Figure 26. Surface porosity profiles for parallel scans with scan spacings of a) 200 µm and b) 250 µm.

In Figure 27, each laser type was tested at various scan spacings, and the maximum temperature was recorded. The maximum temperature from all lasers decreases between 200 µm, with a high degree of overlapping, and 450 µm, with no overlapping, approaching the maximum temperature from a single scan in Table 8.

The maximum temperature caused by the Gaussian laser gradually decreases as scan spacing increases due to a gradual decrease in overlapping between adjacent scans. The top-hat beam starts with a higher maximum temperature than the Gaussian beam, followed by a gradual and then sharp decrease to below Gaussian. The maximum temperatures of the ring and Bessel beams reach a peak at 300 µm where there is more overlapping, but they decrease at higher scan spacings. The ring beam has increasing maximum temperature between 200 µm and 300 µm as the overlap increases. The Bessel beam, having a Gaussian and ring component, shows a decrease between 200 µm and 225 µm followed by an increase. A line is drawn across at 320 °C because this temperature marks the onset of thermal degradation of PA12 and generally SLS processing should not exceed this temperature [21]. The Gaussian and top-hat beams stay within the acceptable temperature range for all scan spacings. However, the ring and Bessel beams with 200 µm spacings already meet this maximum recommended temperature. At certain scan spacings greater than 200 µm, they exceed this temperature by a large margin.

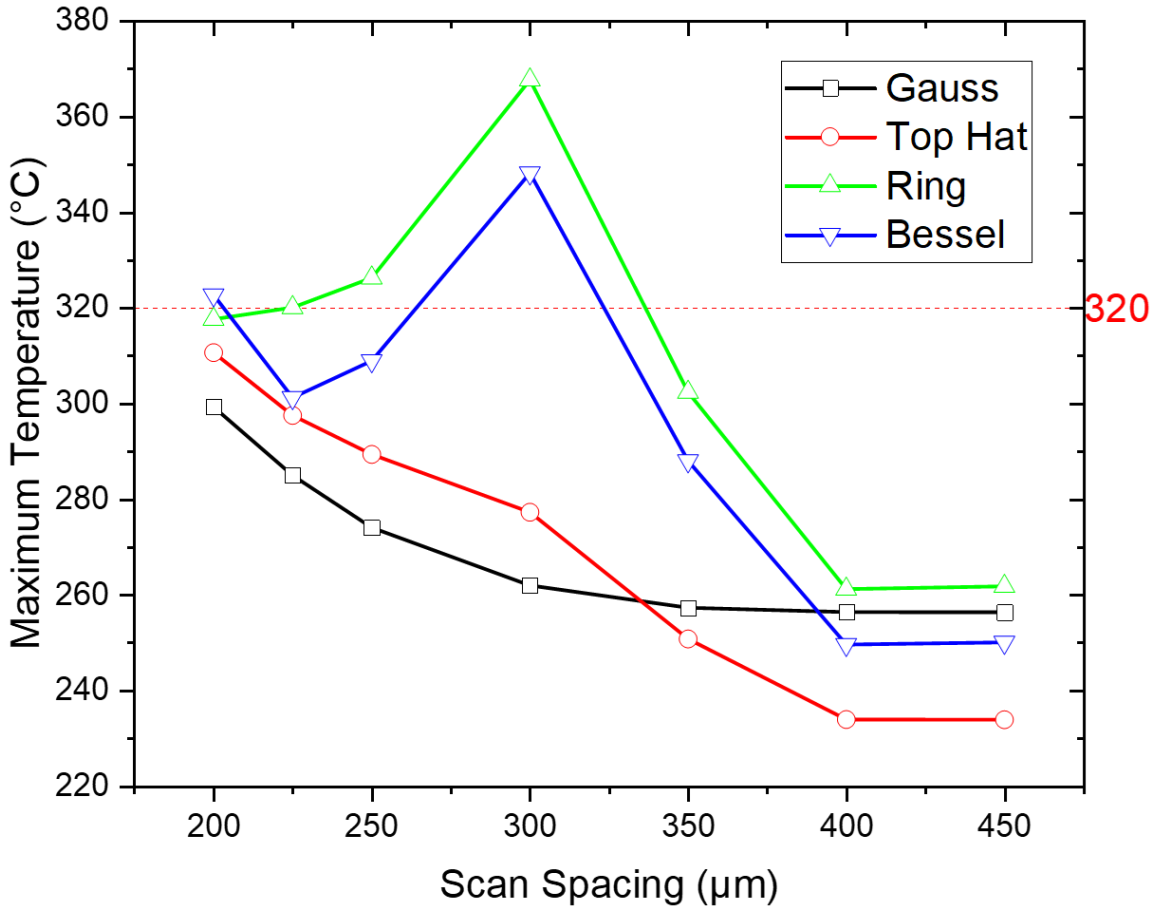

Figure 27. Maximum temperature for parallel scans at various scan spacings for each laser type.

Conclusion

While the different laser beams showed promising results from single scan tests in terms of temperature distributions, maximum temperatures, and porosity profiles, parallel scanning shows emergent phenomena that contribute to higher temperatures, temperature gradients, and anisotropic porosity. As scan spacing increases, the maximum temperature decreases monotonically for the Gaussian and top-hat beams. For the ring and Bessel beams, the maximum temperature increases before decreasing, corresponding to the

amount of overlap. While the Gaussian and top-hat beams generate temperatures well below the degradation threshold, the ring and Bessel beams meet or exceed the threshold in many cases. At the default value of scan spacing (200 μm), the ring and Bessel beams have the potential to cause thermal degradation, limiting the processing window. If these beams are to be used, parameters should be adjusted to reduce maximum temperatures.

Set to default parameters, the Gaussian beam had the lowest temperature and the smallest gradients of the group. The top-hat beam also shows acceptable maximum temperatures and lower predicted porosity than the Gaussian beam, with a relatively smooth porosity profile. While the ring beam results in temperatures near the degradation threshold, the porosity distribution is similar to, albeit higher than, the Gaussian and top-hat beams. Of the laser beams tested at these conditions, the top-hat beam represents the best alternative to the Gaussian beam.

Optimizing the laser intensity distribution requires the consideration of the constructive interference that occurs as the laser scans in one direction and between parallel scans in the other direction. These geometric parameters determine the arrangement of local maxima and minima of temperature, which cause degradation at the high end and lack of melting and densification at the low end. An ideal temperature distribution within a melt pool would be uniform and high enough to ensure complete melting and densification while not exceeding the degradation threshold. Future works may aim to produce more uniform melt pool temperatures by exploring the parameter space systematically.

CHAPTER FIVE

CONCLUSION

Process-Structure-Property-Performance Modeling

The SLS process model developed in Chapter Two accurately predicts the density evolution of the powder as it forms into a solid part. It captures the relationship between process parameters and final density. Through representative volume elements, the process outcome is linked with a mechanical model, and a process-structure-property-performance framework is established.

Thermal Degradation in the Melt Pool

Through thermogravimetric analysis, the chemical kinetics of the degradation of PA12 are quantified. A temperature dependent chemical reaction model is implemented alongside the SLS process model in Chapter Three. Simulating SLS at different laser powers provided insight into the degree of conversion and subsequent mass loss resulting from degradation. However, even with laser powers set to triple the recommended value, the amount of mass loss has a negligible effect on the thermal properties of the melt pool.

Expanding the Processing Window with Laser Beam Shaping

Chapter Four, exploring the effect of laser beam profiles on temperature and porosity, finds that the top-hat, ring, and Bessel beams can result in higher temperatures than a Gaussian beam operating at the same conditions. Furthermore, due to the overlapping of parallel scans, the ring and Bessel beams may result in temperatures beyond the degradation threshold. While the maximum temperatures resulting from the Gaussian and top-hat beams are inversely proportional to scan spacing, that of the ring

and Bessel beams may increase as scan spacing increases. For the conditions tested, the Gaussian beam generally provided the most uniform temperature distribution, and the top-hat beam provided acceptable temperatures. The Gaussian, top-hat, and ring beams resulted in similar porosity profiles when tested at recommended settings, however the Bessel beam showed periodic variations in the porosity profile. At the conditions tested, the top-hat beam is predicted to be the best alternative to the Gaussian beam.

Future Outlook

The process model's limitations include its reliance on property data from various grades of PA12 powder, condensation of powder property distributions into singular values, simplifications in fluid dynamics, a time-based termination criterion for densification, generalizations of thermal history, and a simplified representation of phases. Future models may benefit from:

- More comprehensive material characterization
- Discrete powder particles with a distribution of properties
- Explicit modeling of fluid dynamics
- A more advanced understanding of the termination criteria that govern densification
- Extended and varied thermal histories
- The modeling of multiple crystal phases

Future work may explore the framework through a top-down approach that tailors the process parameters to induce a desired material structure, like in [7].

The thermal degradation model could be improved by including additional reactions such as oxidation, chain scission, and pyrolysis. Expanding model validity to a higher temperature range may increase model accuracy for high energy densities.

A systematic investigation of the process parameter space and laser beam profiles may lead to more uniform melt pool temperature distributions.

APPENDICES

Appendix A

List of Symbols and Values

Table A-1: List of symbols and values.

Symbol	Description
A	Absorptivity (1 – reflectivity)
A_0	Area of cross-section
a_0	Initial pore radius
C_p	Specific heat capacity
dt	Time step size
E_a	Activation energy for viscosity
E_v	Volumetric energy density
F	Farz factor
G	Nakamura function
H_χ	Heat of crystallization/melting
h	Convective heat transfer coefficient
K_c	Nonisothermal crystallization rate
K_0	Growth rate constant
K_g	Nucleation rate constant
k	Avrami rate constant
L	Layer height
n	Avrami exponent
$\boldsymbol{P}$	Laser power
$\boldsymbol{q_c}$	Convective heat flux
$\boldsymbol{q_\ell}$	Instantaneous laser intensity distribution
$\overline{\boldsymbol{q_\ell}}$	Time averaged laser intensity distribution
R	Universal gas constant
r_0	Initial particle radius
r_x, r_y	Laser radius in x and y directions
S	Scan spacing
T	Temperature
T_0	Equilibrium melting temperature
T_a	Ambient temperature
T_c	Isothermal crystallization temperature
T_g	Glass transition temperature
T_∞	Lower temperature limit for crystallization
T_{ref}	Reference temperature for viscosity
t	Time

$t_{½}$	Crystallization half time
U	Activation energy for crystallization
v	Laser fill scan velocity
x	Primary Cartesian axis, length
y	Secondary Cartesian axis, width
z	Tertiary Cartesian axis, height
x_ω	Primary laser axis, length
y_ω	Secondary laser axis, width
α	Relative crystallinity
β	Extinction coefficient
Γ	Surface tension
ΔH	Heat of melting
η	Viscosity
η_{ref}	Viscosity at reference temperature
θ	Sintering growth angle
Λ	Maxwell model constant
λ	Thermal conductivity
λ_s, λ_g	Thermal conductivity of solid and gas
ρ	Density
ρ_b	Bulk density
ρ_t	Tap density
τ	Stress relaxation time
τ_A	Relaxation time pre-exponential factor
τ_B	Relaxation time exponential factor
φ	Porosity
φ_0	Initial porosity
χ	Absolute crystallinity
χ_0	Absolute crystallinity at initial condition
χ_{max}	Maximum absolute crystallinity
ω	Laser traversal angle

Appendix B

Experimental Measurements of Density

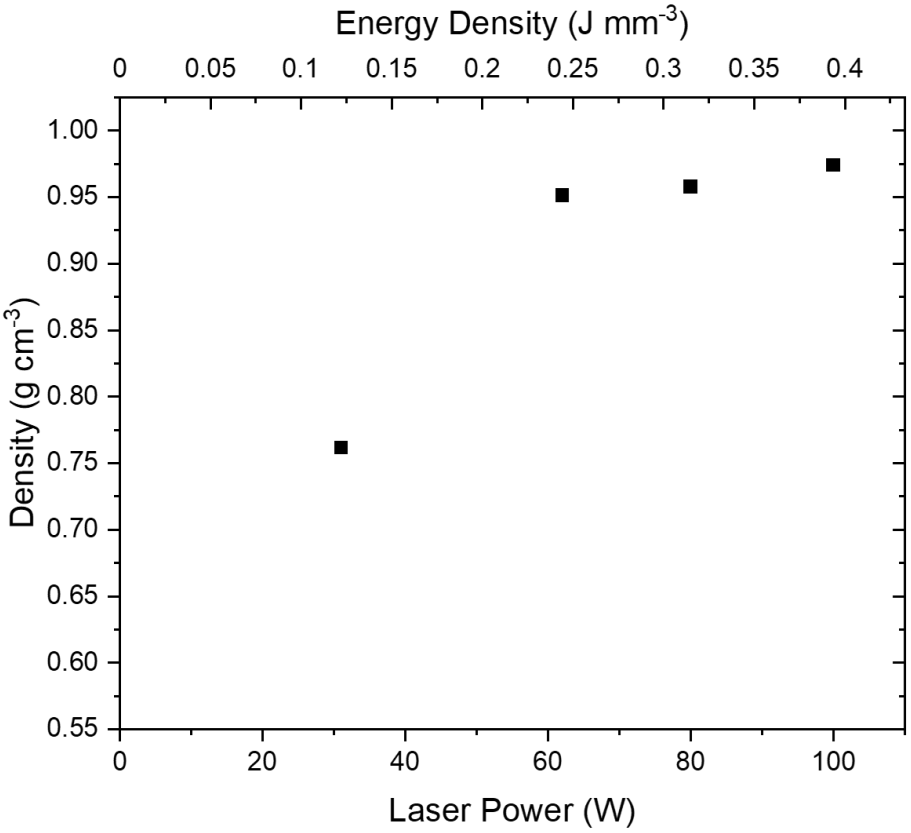

Figure B-1. Density of rectangular sections cut from coupons produced at different laser powers.

Appendix C

Experimental Measurements of Heat of Melting

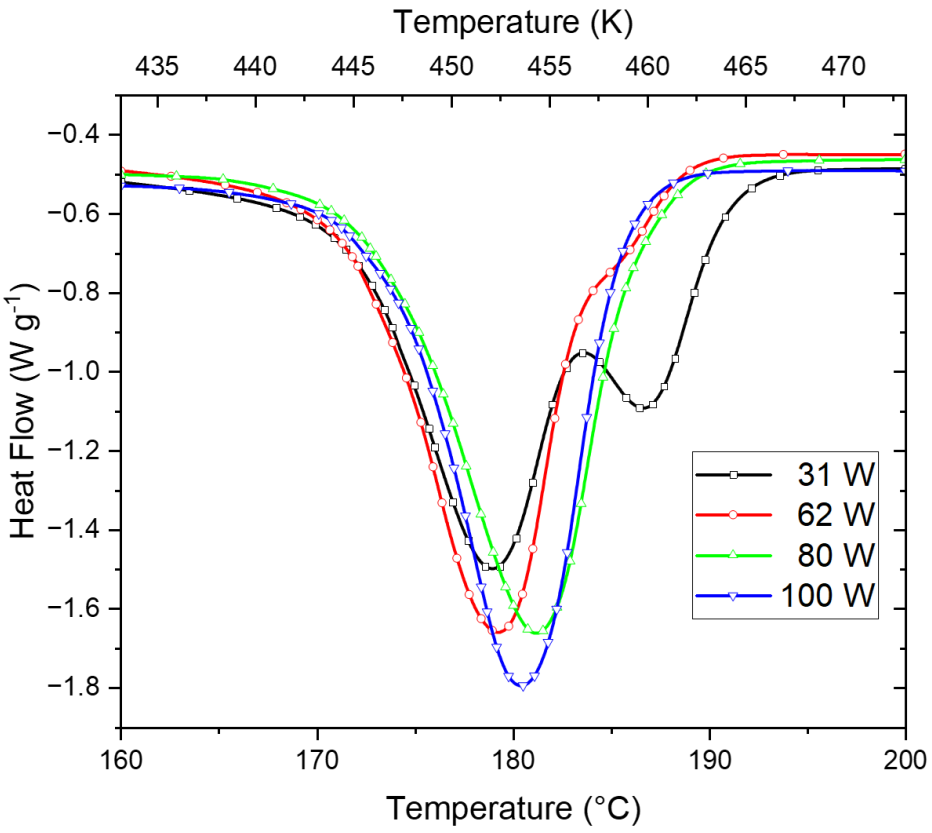

Figure C-1. Normalized heat flow through the melting temperature of coupons produced at different laser powers.

Appendix D

Degradation Plots

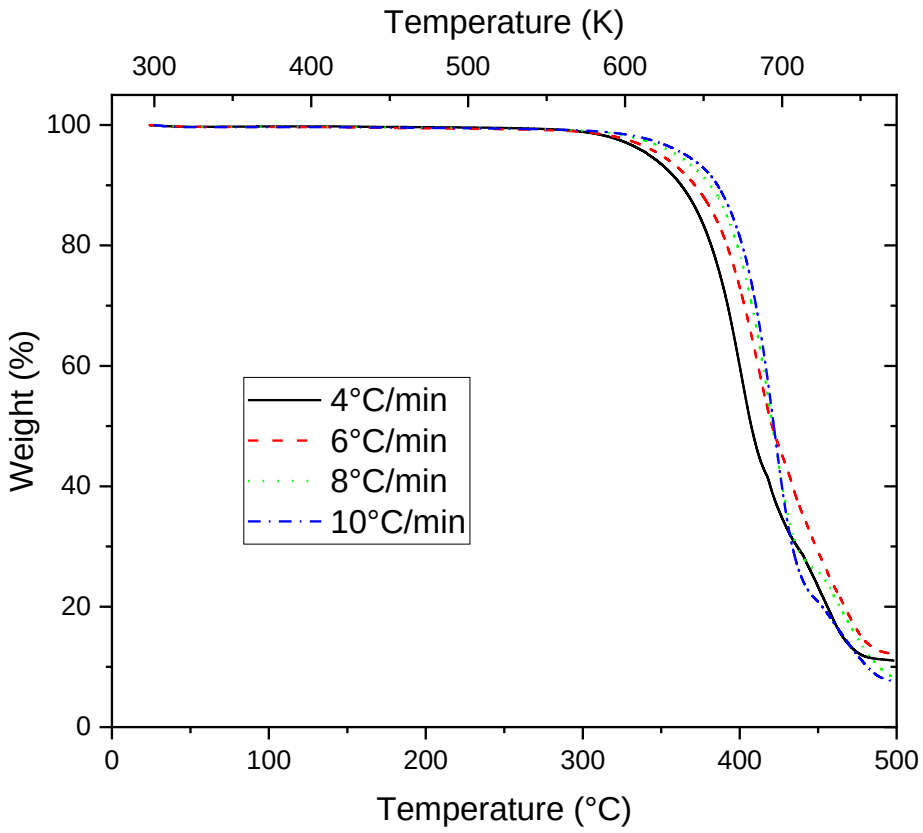

Figure D-1: Full plot of experimental TGA data for degradation of PA12.

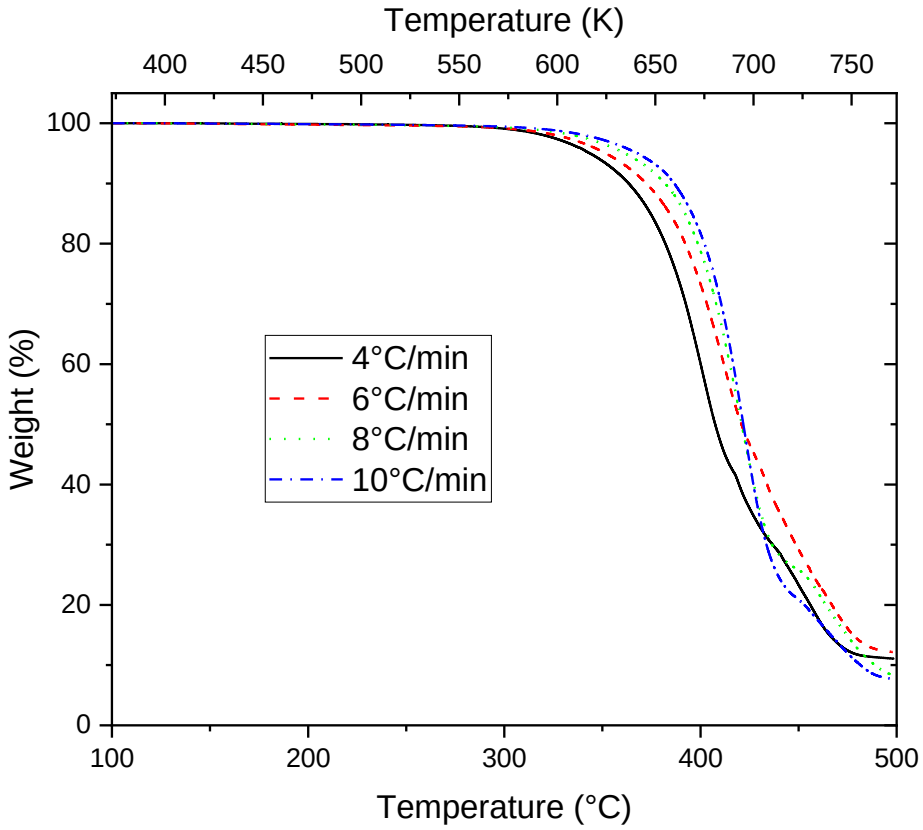

Figure D-2: Full plot of moisture adjusted TGA data for degradation of PA12.

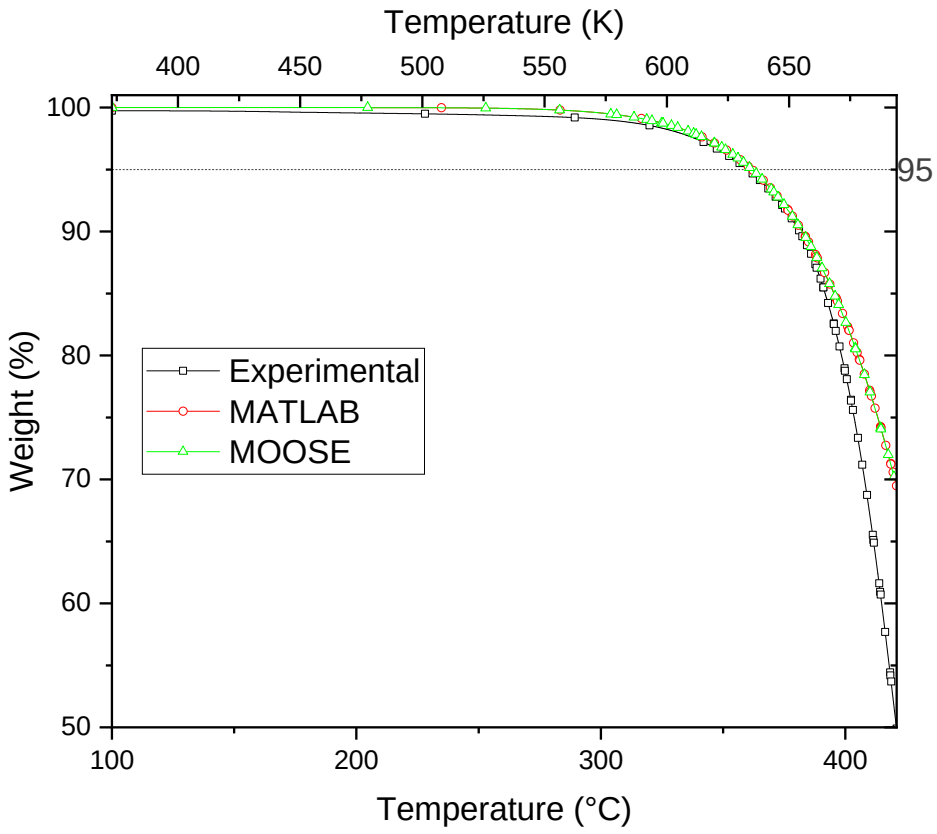

Figure D-3: Full plot comparing experimental data to modeling predictions for degradation of PA12.

REFERENCES

[1] I. Gibson, D. W. Rosen, B. Stucker, and M. Khorasani, *Additive Manufacturing Technologies*, vol. 0, no. 3. Springer, Cham, 2021. doi: 10.2207/jjws.89.82.

[2] C. A. Chatham, T. E. Long, and C. B. Williams, "A review of the process physics and material screening methods for polymer powder bed fusion additive manufacturing," *Prog. Polym. Sci.*, vol. 93, pp. 68–95, 2019, doi: 10.1016/j.progpolymsci.2019.03.003.

[3] A. Kafle, E. Luis, R. Silwal, H. M. Pan, P. L. Shrestha, and A. K. Bastola, "3D / 4D Printing of Polymers : Fused Deposition Modelling (FDM), Selective Laser Sintering (SLS), and Stereolithography (SLA)," *Polymers (Basel).*, vol. 13, pp. 1–37, 2021, doi: 10.3390.

[4] B. Schoinochoritis, D. Chantzis, and K. Salonitis, "Simulation of metallic powder bed additive manufacturing processes with the finite element method: A critical review," *Proc. Inst. Mech. Eng. Part B J. Eng. Manuf.*, vol. 231, no. 1, pp. 96–117, 2017, doi: 10.1177/0954405414567522.

[5] A. Bauereiß, T. Scharowsky, and C. Körner, "Defect generation and propagation mechanism during additive manufacturing by selective beam melting," *J. Mater. Process. Technol.*, vol. 214, no. 11, pp. 2522–2528, Nov. 2014, doi: 10.1016/J.JMATPROTEC.2014.05.002.

[6] I. Yadroitsau, "Direct manufacturing of 3D objects by selective laser melting of metal powders." Saint-Etienne, 2008.

[7] W. Yan *et al.*, "Data-driven multi-scale multi-physics models to derive process–structure–property relationships for additive manufacturing," *Comput. Mech.*, vol. 61, no. 5, pp. 521–541, 2018, doi: 10.1007/s00466-018-1539-z.

[8] B. Caulfield, P. E. McHugh, and S. Lohfeld, "Dependence of mechanical properties of polyamide components on build parameters in the SLS process," *J. Mater. Process. Technol.*, vol. 182, no. 1–3, pp. 477–488, 2007, doi: 10.1016/j.jmatprotec.2006.09.007.

[9] N. Hopkinson, C. E. Majewski, and H. Zarringhalam, "Quantifying the degree of particle melt in Selective Laser Sintering®," *CIRP Ann.*, vol. 58, no. 1, pp. 197–200, Jan. 2009, doi: 10.1016/J.CIRP.2009.03.001.

[10] T. L. Starr, T. J. Gornet, and J. S. Usher, "The effect of process conditions on mechanical properties of laser-sintered nylon," *Rapid Prototyp. J.*, 2011.

[11] M. Vasquez, B. Haworth, and N. Hopkinson, "Methods for quantifying the stable sintering region in laser sintered polyamide-12," *Polym. Eng. Sci.*, vol. 53, no. 6, pp. 1230–1240, Jun. 2013, doi: 10.1002/pen.23386.

[12] C. A. Chatham, M. J. Bortner, B. N. Johnson, T. E. Long, and C. B. Williams, "Predicting mechanical property plateau in laser polymer powder bed fusion additive manufacturing via the critical coalescence ratio," *Mater. Des.*, vol. 201, p. 109474, 2021, doi: 10.1016/j.matdes.2021.109474.

[13] S. Dupin, O. Lame, C. Barrès, and J. Y. Charmeau, "Microstructural origin of physical and mechanical properties of polyamide 12 processed by laser sintering," *Eur. Polym. J.*, vol. 48, no. 9, pp. 1611–1621, 2012, doi: 10.1016/j.eurpolymj.2012.06.007.

[14] J. Li, S. Yuan, J. Zhu, S. Li, and W. Zhang, “Numerical model and experimental validation for laser sinterable semi-crystalline polymer: Shrinkage and warping,” *Polymers (Basel).*, vol. 12, no. 6, 2020, doi: 10.3390/POLYM12061373.

[15] D. Soldner, S. Greiner, C. Burkhardt, D. Drummer, P. Steinmann, and J. Mergheim, “Numerical and experimental investigation of the isothermal assumption in selective laser sintering of PA12,” *Addit. Manuf.*, vol. 37, p. 101676, Jan. 2021, doi: 10.1016/j.addma.2020.101676.

[16] A. Mokrane, M. Boutaous, and S. Xin, “Process of selective laser sintering of polymer powders: Modeling, simulation, and validation,” *Comptes Rendus Mécanique*, vol. 346, no. 11, pp. 1087–1103, Nov. 2018, doi: 10.1016/J.CRME.2018.08.002.

[17] G. Bugeda, M. Cervera, and G. Lombera, “Numerical prediction of temperature and density distributions in selective laser sintering processes,” *Rapid Prototyp. J.*, vol. 5, no. 1, pp. 21–26, 1999, doi: 10.1108/13552549910251846.

[18] L. Xin, M. Boutaous, S. Xin, and D. A. Siginer, “Multiphysical modeling of the heating phase in the polymer powder bed fusion process,” *Addit. Manuf.*, vol. 18, pp. 121–135, Dec. 2017, doi: 10.1016/J.ADDMA.2017.10.006.

[19] M. Ganci, W. Zhu, G. Buffa, L. Fratini, S. Bo, and C. Yan, “A macroscale FEM-based approach for selective laser sintering of thermoplastics,” *Int. J. Adv. Manuf. Technol.*, vol. 91, no. 9–12, pp. 3169–3180, 2017, doi: 10.1007/s00170-017-9998-5.

[20] A. Amado, M. Schmid, and K. Wegener, “Simulation of warpage induced by non-isothermal crystallization of co-polypropylene during the SLS process,” *AIP Conf. Proc.*, vol. 1664, no. 1, p. 160002, May 2015, doi: 10.1063/1.4918509.

[21] A. Wegner and G. Witt, “Understanding the decisive thermal procebes in laser sintering of polyamide 12,” *AIP Conf. Proc.*, vol. 1664, no. May, pp. 1–6, 2015, doi: 10.1063/1.4918511.

[22] D. Bourell, J. Coholich, A. Chalancon, and A. Bhat, “Evaluation of energy density measures and validation for powder bed fusion of polyamide,” *CIRP Ann.*, vol. 66, no. 1, pp. 217–220, Jan. 2017, doi: 10.1016/J.CIRP.2017.04.128.

[23] P. Chen *et al.*, “Systematical mechanism of Polyamide-12 aging and its micro-structural evolution during laser sintering,” *Polym. Test.*, vol. 67, pp. 370–379, May 2018, doi: 10.1016/j.polymertesting.2018.03.035.

[24] K. Wudy, D. Drummer, F. Kühnlein, and M. Drexler, “Influence of degradation behavior of polyamide 12 powders in laser sintering process on produced parts,” *AIP Conf. Proc.*, vol. 1593, no. February 2015, pp. 691–695, 2014, doi: 10.1063/1.4873873.

[25] F. Paolucci, M. J. H. van Mook, L. E. Govaert, and G. W. M. Peters, “Influence of post-condensation on the crystallization kinetics of PA12: From virgin to reused powder,” *Polymer (Guildf).*, vol. 175, pp. 161–170, Jun. 2019, doi: 10.1016/j.polymer.2019.05.009.

[26] K. Wudy and D. Drummer, “Aging effects of polyamide 12 in selective laser sintering: Molecular weight distribution and thermal properties,” *Addit. Manuf.*, vol. 25, no. November 2018, pp. 1–9, 2019, doi: 10.1016/j.addma.2018.11.007.

[27] K. Wudy and D. Drummer, “Aging behavior of polyamide 12: Interrelation between bulk characteristics and part properties,” *Solid Free. Fabr. 2016 Proc. 27th Annu. Int. Solid Free. Fabr. Symp. - An Addit. Manuf. Conf. SFF 2016*, pp. 770–781, 2016.
[28] L. Duddleston, “Polyamide (Nylon) 12 Degradation during the Selective Laser Sintering (SLS) Process: A Quantification for Recycling Optimization”, doi: 10.13140/RG.2.1.3548.8487.
[29] L. J. L. Duddleston, A. T. Puck, A. Harris, N. P. Doll, and T. A. Osswald, “Differential scanning calorimetry (DSC) quantification of polyamide 12 (nylon 12) degradation during the selective laser sintering (SLS) process,” *Annu. Tech. Conf. - ANTEC, Conf. Proc.*, vol. 12, no. Nylon 12, pp. 1–4, 2016.
[30] S. Ghosh, D. Khastgir, A. K. Bhowmick, and P. G. Mukunda, “Thermal degradation and ageing of segmented polyamides,” *Polym. Degrad. Stab.*, vol. 67, no. 3, pp. 427–436, Mar. 2000, doi: 10.1016/S0141-3910(99)00141-X.
[31] T. H. C. Childs, M. Berzins, G. R. Ryder, and A. Tontowi, “Selective laser sintering of an amorphous polymer - Simulations and experiments,” *Proc. Inst. Mech. Eng. Part B J. Eng. Manuf.*, vol. 213, no. 4, pp. 333–349, 1999, doi: 10.1243/0954405991516822.
[32] L. Dong, A. Makradi, S. Ahzi, and Y. Remond, “Three-dimensional transient finite element analysis of the selective laser sintering process,” *J. Mater. Process. Technol.*, vol. 209, no. 2, pp. 700–706, 2009, doi: 10.1016/j.jmatprotec.2008.02.040.
[33] S. Patel and M. Vlasea, “Melting modes in laser powder bed fusion,” *Materialia*, vol. 9, p. 100591, 2020, doi: 10.1016/j.mtla.2020.100591.
[34] T. G. Spears and S. A. Gold, “In-process sensing in selective laser melting (SLM) additive manufacturing,” *Integr. Mater. Manuf. Innov.*, vol. 5, no. 1, pp. 16–40, 2016, doi: 10.1186/s40192-016-0045-4.
[35] A. S. Metel, M. M. Stebulyanin, S. V. Fedorov, and A. A. Okunkova, “Power Density Distribution for Laser Additive Manufacturing (SLM): Potential, Fundamentals and Advanced Applications,” *Technol. 2019, Vol. 7, Page 5*, vol. 7, no. 1, p. 5, Dec. 2018, doi: 10.3390/TECHNOLOGIES7010005.
[36] R. Klein, *Laser Welding of Plastics: materials, processes, and industrial applications*, 1st ed. John Wiley & Sons, 2012.
[37] C. E. Protasov and A. V. Gusarov, “Modeling the Effect of Beam Shaping at Selective Laser Melting,” *Procedia IUTAM*, vol. 23, pp. 147–154, Jan. 2017, doi: 10.1016/J.PIUTAM.2017.06.015.
[38] S. N. Grigoriev *et al.*, “Beam Shaping in Laser Powder Bed Fusion: Peclet Number and Dynamic Simulation,” *Met. 2022, Vol. 12, Page 722*, vol. 12, no. 5, p. 722, Apr. 2022, doi: 10.3390/MET12050722.
[39] J. Grünewald, F. Gehringer, M. Schmöller, and K. Wudy, “Influence of Ring-Shaped Beam Profiles on Process Stability and Productivity in Laser-Based Powder Bed Fusion of AISI 316L,” *Met. 2021, Vol. 11, Page 1989*, vol. 11, no. 12, p. 1989, Dec. 2021, doi: 10.3390/MET11121989.
[40] T. U. Tumkur *et al.*, “Nondiffractive beam shaping for enhanced optothermal

control in metal additive manufacturing," *Sci. Adv.*, vol. 7, no. 38, pp. 9358–9373, Sep. 2021, doi: 10.1126/sciadv.abg9358.
[41] T. T. Roehling *et al.*, "Controlling grain nucleation and morphology by laser beam shaping in metal additive manufacturing," *Mater. Des.*, vol. 195, p. 109071, Oct. 2020, doi: 10.1016/J.MATDES.2020.109071.
[42] M. J. Matthews *et al.*, "Controlling melt pool shape, microstructure and residual stress in additively manufactured metals using modified laser beam profiles," *Procedia CIRP*, vol. 94, pp. 200–204, Jan. 2020, doi: 10.1016/J.PROCIR.2020.09.038.
[43] R. Shi, S. A. Khairallah, T. T. Roehling, T. W. Heo, J. T. McKeown, and M. J. Matthews, "Microstructural control in metal laser powder bed fusion additive manufacturing using laser beam shaping strategy," *Acta Mater.*, vol. 184, pp. 284–305, Feb. 2020, doi: 10.1016/J.ACTAMAT.2019.11.053.
[44] R. Moore, G. Orlandi, T. Rodgers, D. Moser, H. Murdoch, and F. Abdeljawad, "Microstructure-Based Modeling of Laser Beam Shaping During Additive Manufacturing," *JOM*, vol. 76, no. 3, pp. 1726–1736, Mar. 2024, doi: 10.1007/S11837-023-06363-8/FIGURES/7.
[45] G. Craft, J. Nussbaum, N. Crane, and J. P. Harmon, "Impact of extended sintering times on mechanical properties in PA-12 parts produced by powderbed fusion processes," *Addit. Manuf.*, vol. 22, no. July, pp. 800–806, 2018, doi: 10.1016/j.addma.2018.06.028.
[46] S. C. Ligon, R. Liska, J. Stampfl, M. Gurr, and R. Mülhaupt, "Polymers for 3D Printing and Customized Additive Manufacturing," *Chem. Rev.*, vol. 117, no. 15, pp. 10212–10290, 2017, doi: 10.1021/acs.chemrev.7b00074.
[47] R. D. Goodridge, C. J. Tuck, and R. J. M. Hague, "Laser sintering of polyamides and other polymers," *Prog. Mater. Sci.*, vol. 57, no. 2, pp. 229–267, 2012, doi: 10.1016/j.pmatsci.2011.04.001.
[48] T. Instruments, "Heat Capacity Measurements Using Modulated DSC (MDSC) – Both Ramping and Quasi-isothermal Methods," pp. 1–2.
[49] H. Zarringhalam, C. Majewski, and N. Hopkinson, "Degree of particle melt in Nylon-12 selective laser-sintered parts," *Rapid Prototyp. J.*, vol. 15, no. 2, pp. 126–132, 2009, doi: 10.1108/13552540910943423.
[50] S. Gogolewski, K. Czerntawska, and M. Gastorek, "Effect of annealing on thermal properties and crystalline structure of polyamides. Nylon 12 (polylaurolactam)," *Colloid Polym. Sci. Kolloid Zeitschrift Zeitschrift für Polym.*, vol. 258, no. 10, pp. 1130–1136, 1980, doi: 10.1007/BF01382456.
[51] J. C. Russ and R. T. Dehoff, *Practical stereology*. Springer Science & Business Media, 2012.
[52] J. Goldak, A. Chakravarti, and M. Bibby, "A new finite element model for welding heat sources," *Metall. Trans. B 1984 152*, vol. 15, no. 2, pp. 299–305, Jun. 1984, doi: 10.1007/BF02667333.
[53] P. Peyre, Y. Rouchausse, D. Defauchy, and G. Régnier, "Experimental and numerical analysis of the selective laser sintering (SLS) of PA12 and PEKK semi-crystalline polymers," *J. Mater. Process. Technol.*, vol. 225, pp. 326–336, 2015,

doi: 10.1016/j.jmatprotec.2015.04.030.
[54] M. TG, P. S, and P. J, “The Bouguer-Beer-Lambert Law: Shining Light on the Obscure,” *Chemphyschem*, vol. 21, no. 18, 2020, doi: 10.1002/CPHC.202000464.
[55] J. R. Howell, M. P. Menguc, and R. Siegel, *Thermal Radiation Heat Transfer*. CRC Press, 2010. doi: 10.1201/9781439894552.
[56] A. Iveković, M. L. Montero-Sistiaga, J. Vleugels, J. P. Kruth, and K. Vanmeensel, “Crack mitigation in Laser Powder Bed Fusion processed Hastelloy X using a combined numerical-experimental approach,” *J. Alloys Compd.*, vol. 864, p. 158803, May 2021, doi: 10.1016/J.JALLCOM.2021.158803.
[57] T. Laumer, T. Stichel, K. Nagulin, and M. Schmidt, “Optical analysis of polymer powder materials for Selective Laser Sintering,” *Polym. Test.*, vol. 56, pp. 207–213, Dec. 2016, doi: 10.1016/J.POLYMERTESTING.2016.10.010.
[58] R. Courant, K. Friedrichs, and H. Lewy, “Über die partiellen Differenzengleichungen der mathematischen Physik,” *Math. Ann.*, vol. 100, no. 1, pp. 32–74, Dec. 1928, doi: 10.1007/BF01448839.
[59] J. Irwin and P. Michaleris, “A Line Heat Input Model for Additive Manufacturing,” *J. Manuf. Sci. Eng. Trans. ASME*, vol. 138, no. 11, Nov. 2016, doi: 10.1115/1.4033662.
[60] D. W. Van Krevelen and K. Te Nijenhuis, *Properties of Polymers Their Correlation with Chemical Structure; their Numerical Estimation and Prediction from Additive Group Contributions*, Fourth. 2009. doi: 10.1016/b978-0-08-054819-7.00027-3.
[61] K. Nakamura, T. Watanabe, K. Katayama, and T. Amano, “Some aspects of nonisothermal crystallization of polymers. I. Relationship between crystallization temperature, crystallinity, and cooling conditions,” *J. Appl. Polym. Sci.*, vol. 16, no. 5, pp. 1077–1091, May 1972, doi: 10.1002/APP.1972.070160503.
[62] M. Avrami, “Kinetics of Phase Change. I General Theory,” *J. Chem. Phys.*, vol. 7, no. 12, pp. 1103–1112, Dec. 1939, doi: 10.1063/1.1750380.
[63] M. Zhao, K. Wudy, and D. Drummer, “Crystallization kinetics of polyamide 12 during Selective laser sintering,” *Polymers (Basel).*, vol. 10, no. 2, 2018, doi: 10.3390/polym10020168.
[64] F. Neugebauer, V. Ploshikhin, J. Ambrosy, and G. Witt, “Isothermal and non-isothermal crystallization kinetics of polyamide 12 used in laser sintering,” *J. Therm. Anal. Calorim.*, vol. 124, no. 2, pp. 925–933, May 2016, doi: 10.1007/S10973-015-5214-8/FIGURES/9.
[65] J. D. Hoffman, G. T. Davis, and J. I. Lauritzen, “The Rate of Crystallization of Linear Polymers with Chain Folding BT - Treatise on Solid State Chemistry: Volume 3 Crystalline and Noncrystalline Solids,” N. B. Hannay, Ed., Boston, MA: Springer US, 1976, pp. 497–614. doi: 10.1007/978-1-4684-2664-9_7.
[66] J. D. Hoffman and J. J. Weeks, “Melting Process and the Equilibrium Melting Temperature of Polychlorotrifluoroethylene,” *J. Res. Natl. Bur. Stand. Sect. A, Phys. Chem.*, vol. 66A, no. 1, p. 13, Jan. 1962, doi: 10.6028/JRES.066A.003.
[67] A. Amado, K. Wegener, M. Schmid, and G. Levy, “Characterization and modeling of non-isothermal crystallization of Polyamide 12 and co-Polypropylene during the

SLS process," *5th Int. Polym. Mould. Innov. Conf.*, p. 60, 2012.
[68] A. Ziabicki, "Fundamentals of fibre formation : the science of fibre spinning and drawing," *(No Title)*, Accessed: Nov. 07, 2023. [Online]. Available: https://cir.nii.ac.jp/crid/1130000795469889920
[69] B. Yao, Z. Li, and F. Zhu, "Effect of powder recycling on anisotropic tensile properties of selective laser sintered PA2200 polyamide," *Eur. Polym. J.*, vol. 141, no. September, p. 110093, 2020, doi: 10.1016/j.eurpolymj.2020.110093.
[70] E. D. Bain, E. J. Garboczi, J. E. Seppala, T. C. Parker, and K. B. Migler, "AMB2018-04: Benchmark Physical Property Measurements for Powder Bed Fusion Additive Manufacturing of Polyamide 12," 2019, doi: 10.1007/s40192-019-00146-3.
[71] L. Verbelen, S. Dadbakhsh, M. Van Den Eynde, J. Kruth, B. Goderis, and P. Van Puyvelde, "Characterization of polyamide powders for determination of laser sintering processability," *Eur. Polym. J.*, vol. 75, pp. 163–174, 2016, doi: 10.1016/j.eurpolymj.2015.12.014.
[72] A. F. Amado Becker, "Characterization and prediction of SLS processability of polymer powders with respect to powder flow and part warpage," ETH Zurich, 2016. doi: https://doi.org/10.3929/ethz-a-010657585 Rights.
[73] J. A. Frenkel, "Viscous flow of crystalline bodies under the action of surface tension," *J. Phys.(USS R)*, vol. 9, no. 5, p. 385, 1945.
[74] C. T. Bellehumeur, M. Kontopoulou, and J. Vlachopoulos, "The role of viscoelasticity in polymer sintering," *Rheol. Acta*, vol. 37, no. 3, pp. 270–278, 1998, doi: 10.1007/s003970050114.
[75] O. ; Pokluda, C. T. ; Bellehumeur, and J. Vlachopoulos, "Modification of Frenkel's model for sintering," *Journal*, vol. 43, 1997.
[76] B. B. Sauer and G. T. Dee, "Surface tension and melt cohesive energy density of polymer melts including high melting and high glass transition polymers," *Macromolecules*, vol. 35, no. 18, pp. 7024–7030, 2002, doi: 10.1021/ma0202437.
[77] P. Hejmady, L. C. A. van Breemen, D. Hermida-Merino, P. D. Anderson, and R. Cardinaels, "Laser sintering of PA12 particles studied by in-situ optical, thermal and X-ray characterization," *Addit. Manuf.*, vol. 52, p. 102624, Apr. 2022, doi: 10.1016/J.ADDMA.2022.102624.
[78] A. Hamidi *et al.*, "Modelling of sintering during rotational moulding of the thermoplastic polymers," *Int. J. Mater. Form.*, vol. 9, no. 4, pp. 519–530, Sep. 2016, doi: 10.1007/S12289-015-1239-6/FIGURES/18.
[79] G. W. SCHERER, "Viscous Sintering of a Bimodal Pore-Size Distribution," *J. Am. Ceram. Soc.*, vol. 67, no. 11, pp. 709–715, 1984, doi: 10.1111/j.1151-2916.1984.tb19506.x.
[80] J. K. Mackenzie and R. Shuttleworth, "A phenomenological theory of sintering," *Proc. Phys. Soc. Sect. B*, vol. 62, no. 12, pp. 833–852, 1949, doi: 10.1088/0370-1301/62/12/310.
[81] R. L. Nuttall and D. C. Ginnings, "Thermal conductivity of nitrogen from 50 to 500 C and 1 to 100 atmospheres," *J. Res. Natl. Bur. Stand. (1934).*, vol. 58, no. 5, p. 271, 1957.

[82] 3D Systems, “DuraForm ® ProX PA,” 2022.
[83] V. R. Voller and C. R. Swaminathan, “GENERAL SOURCE-BASED METHOD FOR SOLIDIFICATION PHASE CHANGE,” *Numer. Heat Transf. Part B Fundam.*, vol. 19, no. 2, pp. 175–189, Jan. 1991, doi: 10.1080/10407799108944962.
[84] C. J. Permann *et al.*, “MOOSE: Enabling massively parallel multiphysics simulation,” *SoftwareX*, vol. 11, p. 100430, Jan. 2020, doi: 10.1016/J.SOFTX.2020.100430.
[85] A. D. Lindsay *et al.*, “2.0 - MOOSE: Enabling massively parallel multiphysics simulation,” *SoftwareX*, vol. 20, p. 101202, Dec. 2022, doi: 10.1016/J.SOFTX.2022.101202.
[86] A. Lindsay *et al.*, “Automatic Differentiation in MetaPhysicL and Its Applications in MOOSE,” *https://doi.org/10.1080/00295450.2020.1838877*, vol. 207, no. 7, pp. 905–922, 2021, doi: 10.1080/00295450.2020.1838877.
[87] T. Ozawa, “Estimation of activation energy by isoconversion methods,” *Thermochim. Acta*, vol. 203, no. C, pp. 159–165, 1992, doi: 10.1016/0040-6031(92)85192-X.
[88] ASTM International, “Standard Test Method for Decomposition Kinetics by Thermogravimetry Using the Ozawa / Flynn / Wall Method,” in *ASTM Standard*, 2018.
[89] K. P. Pramoda, T. S. Chung, S. L. Liu, H. Oikawa, and A. Yamaguchi, “Characterization and thermal degradation of polyimide and polyamide liquid crystalline polymers,” *Polym. Degrad. Stab.*, vol. 67, pp. 365–374, 2000.
[90] S. Bernard, L. Youinou, and P. Gillard, “MIE determination and thermal degradation study of PA12 polymer powder used for laser sintering,” *J. Loss Prev. Process Ind.*, vol. 26, no. 6, pp. 1493–1500, Nov. 2013, doi: 10.1016/j.jlp.2013.10.001.